SAND2018-6044J

Galinstan liquid metal breakup and droplet formation in a shock-induced cross-flow

Yi Chen[a,*], Justin L. Wagner[a], Paul A. Farias[a], Edward P. DeMauro[b], Daniel R. Guildenbecher[a]

[a]*Sandia National Laboratories, P.O. Box 5800, Albuquerque, NM, 87185, USA.*
[b]*Rutgers University, 98 Brett Road, Piscataway, NJ 08854, USA.*

Submitted as a Full-Length Article
Declarations of interest: none
Running Title: **Galinstan liquid metal breakup**

Abstract

Liquid metal breakup processes are important for understanding a variety of physical phenomena including metal powder formation, thermal spray coatings, fragmentation in explosive detonations and metalized propellant combustion. Since the breakup behaviors of liquid metals are not well studied, we experimentally investigate the roles of higher density and fast elastic surface oxide formation on breakup morphology and droplet characteristics. This work compares the column breakup of water with Galinstan, a room-temperature eutectic liquid metal alloy of gallium, indium and tin. A shock tube is used to generate a step change in convective velocity and back-lit imaging is used to classify morphologies for Weber numbers up to 250. Digital in-line holography (DIH) is then used to quantitatively capture droplet size, velocity and three-dimensional position information. Differences in geometry between canonical spherical drops and the liquid columns utilized in this paper are likely responsible for observations of earlier transition Weber numbers and uni-modal droplet volume distributions. Scaling laws indicate that Galinstan and water share similar droplet size-velocity trends and root-normal volume probability distributions. However, measurements indicate that Galinstan breakup occurs earlier in non-dimensional time and produces more non-spherical droplets due to fast oxide formation.

Key words: Liquid Metal, Liquid Breakup, Shock-induced Cross-flow, Galinstan, Digital In-line Holography, Droplet Quantification

1. Introduction

Understanding the mechanisms that drive liquid metal breakup is essential for a variety of applications including metal powder production (Markus et al. 2002, Luo et al. 2012, Mates et al. 2012), thermal spray deposition (Hussary and Heberlein 2001, Chen et al. 2012, Newbery and Grant 2013),

*Corresponding author, *Telephone number:* +1 (505) 845-8280
Email addresses: yichen@sandia.gov (Yi Chen), jwagner@sandia.gov (Justin L. Wagner), pafaria@sandia.gov (Paul A. Farias), edward.demauro@rutgers.edu (Edward P. DeMauro), drguild@sandia.gov (Daniel R. Guildenbecher)

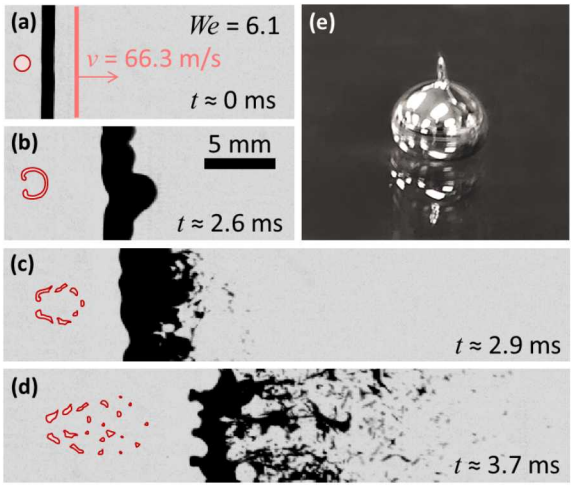

Figure 1: Liquid Galinstan in a shockwave-induced cross-flow is shown during (a) the initial shock arrival, (b) bag formation, (c) bag breakup and (d) column breakup. The inset of each image shows a top-view schematic of the visually estimated breakup morphology, illustrated in shades of red. (e) A single Galinstan droplet illustrates how oxide skin formation prevents the droplet from becoming fully spherical. (Figure available in color online)

conductive microfluidics (Dickey et al. 2008, Liu et al. 2010), metalized solid rocket propellant combustion (Guildenbecher et al. 2014, Chen et al. 2016, 2017b), explosive fragmentation (Rader and Benson 1988, Mingjun et al. 2014), and liquid metal cooling systems (Kondo et al. 1995). In a shock-induced cross-flow, as shown in Fig. 1, the aerodynamic forces imparted by a high speed gas distort the liquid surface while surface tension forces resist deformations. When the the aerodynamic forces exceed surface tension, the liquid breaks apart and forms droplets.

For typical fluids like water, this breakup process has been studied extensively both experimentally and in simulation (Hsiang and Faeth 1992, Joseph et al. 1999, Arienti et al. 2016, Guildenbecher et al. 2017). Several recent numerical investigations have considered high fluid-gas density ratio liquids and liquid metal breakup (Aalburg et al. 2003, Ling et al. 2013, Kékesi et al. 2014, Mingjun et al. 2014, Lin et al. 2015, Yang et al. 2016, Arienti et al. 2017). Aalburg et al. (2003) suggest that for density ratios greater than 32, the density ratio has a minimal effect on deformation and breakup properties. Other simulations by Kékesi et al. (2014), however, indicate that higher density ratios produce faster deformation rates. Performing simulations with liquid metals, Lin et al. (2015) show that high density ratios up to 10,000 lead to higher deformation rates and faster growth of surface waves. Yang et al. (2016) further suggest that a higher density ratio leads to more intensive fragmentation but has a non-monotonic effect on droplet deformation. Because these simulations do not incorporate some important physics related to liquid metals (such as surface oxide formation) and point to disparate conclusions, experimental investigations are needed to help understand the underlying physics. Except for a single experimental data point with mercury (Hsiang and Faeth 1992), there are no known fundamental

experimental investigations of liquid metals in shock-induced cross-flows.

In addition to high densities, most liquid metals also have high surface tensions, low dynamic viscosities, and the ability to form oxide skins. High temperature molten metals can also exhibit complex physical behaviors including the formation of vapor films (Lin et al. 2015), solidification (Manickam et al. 2017), and combustion (Rader and Benson 1988). Studying a liquid metal at room temperature minimizes the effect of heat transfer and combustion while focusing on physics driven by high density ratios and surface mechanics.

Galinstan is a non-toxic, eutectic room-temperature liquid metal alloy. This liquid metal has been utilized as a replacement for mercury in thermometers and for research in energy storage, microfluidics and flexible electronics (Dickey 2014). The material is six times denser than water with a surface tension that is ten times higher. Like aluminum and many other metals, liquid Galinstan forms an oxide skin (Dickey et al. 2008). Figure 1(e) shows a droplet generated by a pipette that quickly formed an oxide skin, preventing it from becoming spherical. The oxide skin is elastic and has a yield stress that can alter the splash impact (Li et al. 2014) or breakup behaviors (Chen et al. 2017a). Because the influence of the oxide skins on breakup is not well-understood, Galinstan can be used to investigate the effects of surface mechanics and density on breakup behavior.

In this work, the breakup morphology and droplet formation statistics of liquid metal Galinstan is compared with water at a variety of Weber numbers. Back-lit imaging provides a qualitative view of the key differences between the two materials. Digital in-line holography (DIH) is then used to provide quantitative measurements of the column deformation as well as droplet velocity and size statistics using automated algorithms. This is the first known paper in archival literature to measure liquid metal breakup in a shock-induced cross-flow. The datasets generated are expected to inform model development and validation while extending scaling relations to liquid metal conditions.

2. Fluid Properties

2.1. Liquid properties

Water is compared with the properties of Galinstan in Table 1. Galinstan (RotoMetals LMP-2) is tertiary eutectic alloy consisting mostly of gallium (68.5%), indium (21.5%) and tin (10%). A eutectic metal melts at a single temperature lower than the melting points of its constituents. Galinstan was chosen for the experiments due to its low toxicity and liquid state at room temperature (melting temperature near -19 °C). The material also essentially has no vapor pressure allowing it to be used in vacuum or in the lab with low inhalation risk. Galinstan has a reported density of $\rho_l = 6440$ kg/m^3 (Karcher et al. 2003), which was confirmed in the laboratory and found to be within 3.4% of the reported value.

Table 1: Properties for Water and Galinstan

Property	Water	Galinstan	Units
Density ρ_l	1000	6440	kg/m^3
Viscosity μ_l	0.89	2.4	$mPa \cdot s$
Surface Tension σ	0.073	0.718	N/m

Surface tension values for Galinstan typically vary from 0.5 to 0.72 N/m depending on measurement conditions. Galinstan quickly forms a thin (5 to 20 $\mathring{A}$) passivating oxide skin (Ga_2O_3 and Ga_2O) with a color that is visually indistinguishable from the fluid in the presence of oxygen above 1 ppm (Regan et al. 1997, Plech et al. 1998, Kim et al. 2013, Dickey 2014). The skin is elastic and once it yields, the material flows freely, forming fresh oxide. Oxide layer formation rates have been studied on long timescales (Plech et al. 1998), but there is currently no experimental data in the literature for oxide formation rates at the timescales relevant to shock-induced aerodynamic breakup. With less than 1 ppm of oxygen, the measured surface tension is approximately 0.533 N/m (Morley et al. 2008, Liu et al. 2010, 2012). In the presence of hydrochloric acid vapor, the surface oxide is replaced with other alloys ($GaCl_3$ and $InCl_3$) permitting the formation of spherical drops; the surface tension is then measured to be 0.524 N/m (Kim et al. 2013).

In most situations, however, oxygen is present and the effects of the surface oxide must be considered. The surface yield stress of eutectic gallium indium with the same Ga_2O_3 and Ga_2O amorphous skin was measured to be approximately 0.5 N/m (Dickey et al. 2008). The elastic component of the oxide skin provides an additional restoring force to droplets on top of the existing surface tension forces. This causes an upward bias in the measured surface tension. In atmosphere, several authors have measured an effective surface tension of approximately $\sigma = 0.718$ N/m (Karcher et al. 2003, Kocourek et al. 2006). To confirm these measurements in the present study, additional pendant drop experiments were performed and measurements indicate that the effective surface tension is within 2.7% of this reported value (Chen et al. 2017a). These experiments were conducted with a syringe in a setup similar to the final liquid delivery system in the shock tube. In addition, the timescales of the pendant drop formation are similar to the timescales of the liquid column formation for shock-induced cross-flow experiments to increase confidence in surface tension measurements. As will be illustrated later from the experimental results, the formation of the elastic oxide layer is sufficiently fast such that the higher effective surface tension value is believed to be applicable during the entire breakup process studied here.

2.2. Non-dimensional scaling

The most important non-dimensional number required for understanding transient liquid breakup behaviors is the Weber number, which compares inertial and surface tension forces,

$$We = \frac{\rho_g u_g^2 d_c}{\sigma}, \tag{1}$$

where ρ_g is the gas density, u_g is the gas velocity, d_c is the diameter of the liquid column, and σ is the surface tension. The Ohnesorge number, which compares viscous and inertial forces, is defined as $Oh = \mu_l/\sqrt{\rho_l \sigma d_c}$, where μ_l is the liquid viscosity and ρ_l is the liquid density. For materials where the Ohnesorge number is small $Oh < 0.1$, such as water ($Oh \approx 0.003$) and liquid metals like Galinstan ($Oh \approx 0.001$), viscous forces are thought to be negligible and the breakup behavior is well described by the Weber number (Hsiang and Faeth 1994, Guildenbecher et al. 2009).

A non-dimensional time, originally derived by Ranger and Nicholls (1969), can be developed from analysis of liquid displacement assuming constant acceleration in the horizontal x-direction due to drag and ignoring y-direction gravity forces. Starting at $t = 0$, a force balance can be generated with $Ma = 1/2 C_d \rho_g u_g^2 A$, where a is the acceleration, M is the mass, C_d is the drag coefficient and A is the the frontal area of the column. Experiments in the literature have shown that 80-95% of the column drag is due to form drag (Hsiang and Faeth 1995). Assuming constant acceleration, $x = 1/2 a t^2$, gives,

$$\frac{x}{d_c} = \frac{C_d}{\pi} \frac{t^2 u_g^2 \rho_g}{d_c^2 \rho_l} = \frac{C_d}{\pi} \tau^2, \tag{2}$$

such that,

$$\tau = \frac{t u_g}{d_c} \sqrt{\frac{\rho_g}{\rho_l}} = \frac{t u_g}{d_c} \frac{1}{\sqrt{\rho^*}}, \tag{3}$$

where t is time and $t = 0$ is the approximate arrival time of the shock wave at the column. The density ratio,

$$\rho^* = \frac{\rho_l}{\rho_g}, \tag{4}$$

is important to incorporate when comparing liquids of different densities (Yim 1996, Yang et al. 2016). Since $\rho^* \gg 1$, virtual mass and Basset history forces can be ignored. This non-dimensional time is most appropriate for initial column acceleration and breakup phenomena. A more detailed derivation of column position, presented in Section 5.2, is required to account for changes in drag force due to changes in the relative velocities of the gas and column.

3. Experimental methods

3.1. Multiphase shock tube

Studying transient behaviors of liquid breakup requires the ability to impose fast changes in gas velocities. A shock tube is capable of producing shock waves that are accompanied by fast changes in

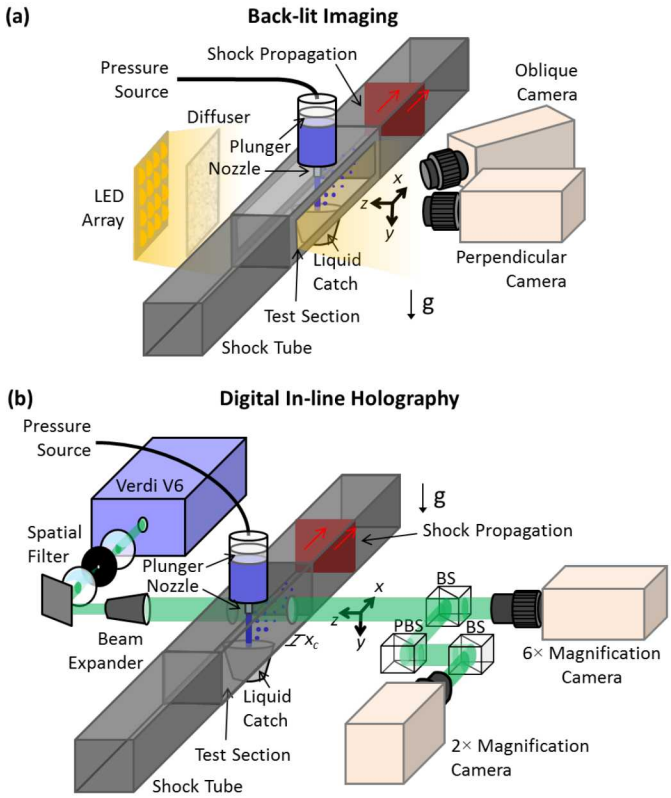

Figure 2: Shock tube and imaging setups are shown. The shock propagates from the driver section and fast-action valve (not shown) down to the driven section before reaching the test section (shockwave travels left to right). The liquid column is generated from an air pressure source and plunger that pushes the fluid through the test section into a liquid catch. (a) For back-lit experiments, an LED array and diffuser are used. (b) For DIH, a single continuous wave laser beam is passed through a spatial filter, beam expander, test section, beam splitters (BS), and polarizing beam splitters (PBS) before being captured by two high-speed cameras. (Figure available in color online)

convective velocity in the gas directly behind the shock boundary. The Multiphase Shock Tube (MST) at Sandia National Laboratories has a 76 $\times$ 76 mm square cross-section and is approximately 5.2 m long (Wagner et al. 2012, Guildenbecher et al. 2016b, DeMauro et al. 2017). The shock tube is driven by pressurized nitrogen, which is released by a fast action valve. Initial experiments were performed with a Dynamics Systems Research model 183-1.5-200 fast action valve. Compared to traditional burst disks, the fast action valve greatly simplifies timing and triggering. However, as discussed in Wagner et al. (2016), this particular valve also has a relatively small, 38 mm throat, leading to flow restrictions and some non-ideal initial conditions. During the course of the experimental campaign, this was replaced with a new valve (Dynamic Systems Research model 725-3.0-6000), which has a larger 76 mm throat. However, due to time limitations not all conditions could be repeated with this new value. Consequently, all water results given here were performed with the initial small valve, while all Galinstan results were performed with the new large valve.

The driven gas in the shock tube is air at 300 K and 84.1 kPa (ambient pressure in Albuquerque,

New Mexico). As the shock tube is fired, the valve opens and a planar shock wave travels down the length of the tube. The convective flow that immediately follows acts as a step change in gas velocity, which interacts with the liquid. The shock wave then reflects off the end wall and travels back through the test section producing near-zero convective gas velocity as it passes (Wagner et al. 2015). Typical Mach numbers for these experiments ranged from 1 to 1.5 and test times ranged from 5 to 10 ms.

Since timing the arrival of a shock with a falling droplet can be challenging, laminar jets (or columns) of liquid were instead investigated. The jet is established using a reservoir and precision fluid dispensing system (Nordson EFD Performus fluid pump), which is triggered to dispense small quantities of fluid driven by a pressurized air source. The air source (at 1 to 8 $psig$) fills the top of the syringe driving down the plunger to dispense a liquid column (0.5 to 1.17 mm diameter) through the tip. The vertical stream velocities were measured to be 1.8 ± 0.4 m/s (mean and standard deviation) for deionized water and 1.8 ± 0.1 m/s for Galinstan. This is significantly less than the convective velocity of the flow behind the shocks and is neglected in the analysis.

The layout of the experiment is shown in Fig. 2. Because Galinstan wets to glass and reacts with aluminum (Morley et al. 2008), additional precautions were required to prepare the instrumentation before an experiment. Large acrylic windows were used for the back-lit experiments, smaller 25 mm diameter $\lambda/10$ flatness glass windows were used for the DIH experiments, and the internal shock tube walls were covered. Where possible, aluminum test section parts were replaced with stainless steel.

3.2. Back-lit and DIH imaging

Two different imaging techniques were applied to characterize the flow. First, a set of back-lit experiments were implemented using a LED array and ground glass diffuser. Video images were captured using two Photron SA-Z high speed cameras sampling at 100 kHz, as shown in Fig. 2(a). One camera is placed perpendicular to the flow while the second camera is placed in an oblique orientation. These experiments are designed to characterize flow morphologies.

Higher magnifications are needed to characterize small droplets. Conventional high magnification imaging often results in out-of-focus features. Digital in-line holography, on the other hand, numerically refocuses the captured diffraction pattern images and is able to quantitatively measure droplet sizes and three-dimensional positions from a single snapshot image (Katz and Sheng 2010). Here, DIH is used to characterize droplet position, shape, size and velocity. The optics required for the DIH experiment are illustrated in Fig. 2(b). A continuous Coherent Verdi V6 laser illuminates the droplets at 532 nm. The light is spatially filtered using a 100 μm pinhole, beam expanded with a $f = 125$ mm and $f = 400$ mm lens pair, and then further expanded (Thorlabs GBE03-A) to create uniform illumination. Diffraction patterns form when the beam traverses over the droplets and are imaged on the opposite side of the shock tube with two high-speed cameras using $2\times$ and $6\times$ magnifications with 0.25 μs exposures. The

2× camera is used to track droplets over time (100 kHz with 640×280 pixels and a minimum detectable droplet diameter ∼40 μm) and the 6× camera provides spatial resolution to measure smaller droplets (20 kHz with 1024×1024 pixels and a minimum detectable droplet diameter ∼12 μm).

DIH records the diffraction patterns created by coherent light interference with light scattered by objects or droplets. After an experiment, the two dimensional (x and y) DIH images are numerically refocused along the optical depth z using,

$$E(x, y; z) = [h(x, y)E_r^*(x, y)] \otimes \gamma(x, y; z), \tag{5}$$

where E is the reconstructed complex amplitude at z, h is the recorded hologram, E_r^* is the conjugate reference wave that is assumed to be planar, $\otimes$ is the convolution operator, and γ is the diffraction kernel. The amplitude $A = |E|$ is then used to visualize the refocused image. By varying z, refocused droplet images are obtained at the original droplet locations. To automatically determine the depth at which each droplet is in focus, a hybrid method using the minimum amplitude and maximum Tenengrad is used to find initial estimates of size and location. A refinement step is implemented to improve the z estimates, followed by additional refinement to remove falsely detected and overlapped droplets. Further details on the processing methods are provided by Gao et al. (2013, 2014) and Guildenbecher et al. (2013). Here data are processed using Sandia National Laboratory's ODIN high capacity MATLAB graphical processing unit accelerated cluster.

After each frame is processed, tracking is used to calculate droplet velocities from the 2× magnification data. The algorithm uses a cost function that looks for nearest neighbors in the next frame that also have similar droplet diameters. Iteration is used to combine similar non-overlapping trajectories. Further details on this algorithm are provided in Guildenbecher et al. (2016a).

This multi-frame tracking method tends to produce accurate three-dimensional velocity measurements and size-velocity correlations. However, especially in regions of dense particle concentration, a significant fraction of the particles may not be successfully tracked, resulting in under-counting of the total mass and potential biases in size distributions for the 2× data. This is improved by combining information with the higher magnification 6× data, where individual drops are more easily segmented. Further details are provided in Section 6.3 and Chen and Guildenbecher (2017).

4. Break-up Morphology

Back-lit imaging is first conducted for water and Galinstan columns at similar Weber numbers as shown in Fig. 3. A high-speed video summary of this back-lit data is included with this paper in Video 1. Previous results in the literature (Igra and Takayama 2001, Igra et al. 2002) suggest that column breakup and spherical drop breakup display minimal differences. However, some differences

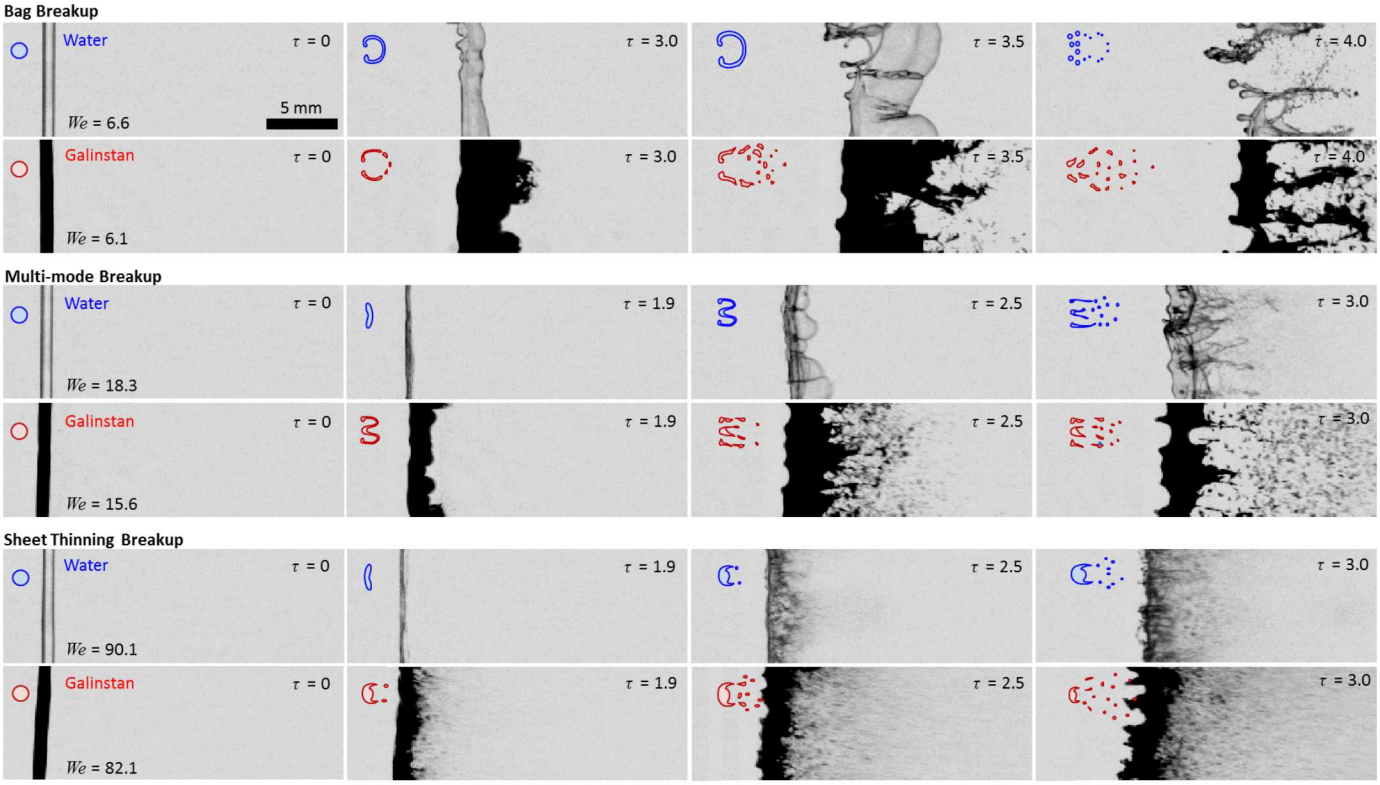

Figure 3: Breakup morphologies for water and Galinstan show three distinct breakup modes using back-lit imaging of 0.84 mm diameter columns. From top to bottom, the bag, multi-mode and sheet thinning modes are shown at the Weber numbers indicated. The inset of each breakup image shows a top-view schematic of the visually estimated breakup morphology using the oblique and perpendicular cameras. A high-speed video summary of this data is included with this paper in Video 1. (Figure available in color online)

between the breakup characteristics of these two geometries are noted in the experimental results and are later discussed in Section 4.4.

Before the arrival of the shockwave, the 0.84 mm diameter columns show some slight deviations from a cylindrical shape. This is likely due to a capillary instability with a most unstable wavelength of $4.5d_c$ (Rayleigh 1878). With a higher surface tension, Galinstan exhibits a more pronounced instability growth rate. As the shock passes the column, these small deviations in diameter have some effect on the local Weber number, thereby slightly increasing the measurement uncertainty. This effect is noticeable in Fig. 3 for Galinstan columns.

Breakup morphology results are described in Fig. 3 for bag, multi-mode, and sheet thinning cases. In bag breakup, the center of the column is first compressed and then expands quickly in the streamwise direction forming a single bag for each horizontal slice, which is confirmed with the oblique camera videos. Eventually, the bag ruptures causing small droplets to form. The remaining portions of the column also break up into larger droplets. In multi-mode breakup, several smaller bags form at each

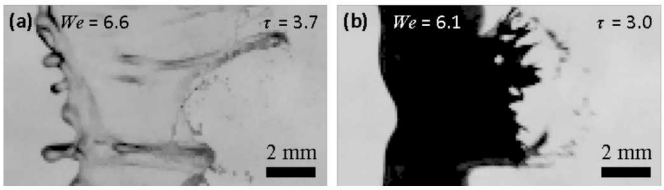

Figure 4: (a) Water and (b) Galinstan morphology during initial bag breakup showing the differences in fragmentation and droplet shapes. The size difference between the bags of the two fluids and the prominence of nodes on the upstream or left-hand side of the water experiment are also clearly illustrated.

horizontal position in the column with ligaments between the bags. Finally, the sheet thinning regime is characterized by an inverted hemispherical column shape with liquid shedding off the edges of the column, generating droplets directly. The core of the column continues to generate droplets as it is accelerated by the convective flow.

4.1. Morphology Comparison

When comparing Galinstan and water at these conditions, it is clear that the upstream side (left or windward side with the forward stagnation point) of the column matches well as a function of non-dimensional time for all test conditions. This indicates that the columns have similar drag properties and that the choice of non-dimensional time is appropriate for the column behavior. In addition, the breakup morphology stages are similar as We is varied.

The overall breakup, on the other hand, occurs earlier in non-dimensional time for Galinstan than for water. This is illustrated in all three cases with breakup and droplet generation appearing at least $\tau = 0.5$ earlier for Galinstan. This earlier breakup result has not been observed in the literature for sprays with varying density ratios (Chou et al. 1997, Chou and Faeth 1998). One potential explanation is that this is driven by the surface oxide yield stress and non-uniformities in liquid Galinstan, which have been incorporated into the effective surface tension value. When the surface oxide yields, the oxide-free surface tension is temporarily lower and the liquid metal beneath begins to flow more freely. If deformation rates exceed the new oxide formation rate, then the effective surface tension of Galinstan will be lower, which would accelerate deformation compared to a constant surface tension. This mechanism may cause the breakup to occur earlier than for typical liquids.

The full extension of the bags in the top row ($We \approx 6.3$) are also much larger for water at $\tau = 3.5$ versus Galinstan at $\tau = 3.0$. A similar phenomenon is observed in multi-mode breakup. This is an indication that either the Galinstan bag thickness is larger or that there is more liquid volume in the remaining column and nodes. If Galinstan bags are thicker, then slightly larger droplet sizes would be expected in the early Galinstan DIH measurements. In addition, the shape of the bags during breakup are also different. For typical fluids, bag breakup is postulated to occur when thicknesses stretch below a critical value, leading to the formation of holes that quickly grow due to surface

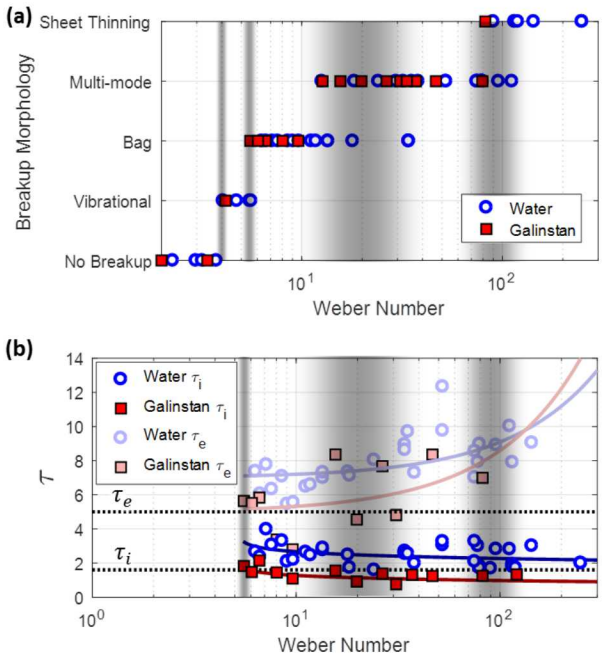

Figure 5: (a) Column breakup morphology is classified as a function of Weber number for water and Galinstan. Areas of ambiguity in classification where multiple morphologies can be observed are shown in gray. Reynolds numbers range from 600 to 2.3×10^4. (b) Breakup initiation times τ_i and end times τ_e are plotted as a function of Weber number. The solid lines are empirical fits (similar to Pilch and Erdman (1987)) and the dotted black lines are simple correlations developed for typical fluids starting from spherical drops by Hsiang and Faeth (1992). (Figure available in color online)

tension (Dombrowski and Hooper 1962, Chou and Faeth 1998). For water in Fig. 4, the bags appear to break up from a small hole, which opens quickly allowing droplets to bead up along the edges (see also Fig. 3, $We \approx 6.3$, $\tau = 4.0$). For Galinstan, the breakup of the bags does not show a beading effect. Rather, the bags appear to break open, akin to fractures seen in solid mechanics, suggesting that mechanisms for fragmentation could differ for the two fluids. Subsequently, the gas behind the liquid forces the bag open and the fractured sections are ejected as non-spherical droplets. The oxide layer, which has a finite thickness, forms quickly. This mechanism prevents smaller droplets from reaching spherical, minimum energy shapes over time (Dickey et al. 2008, Kim et al. 2013). The successful bag expansion that later produces oxide-covered non-spherical droplets (at $t \approx 3$ ms in Fig. 1(c))) would suggest sufficiently fast oxide formation to alter droplet shapes on the millisecond timescale or faster. Finally, it should be noted that liquid metal Galinstan is optically opaque whereas water is translucent. Therefore, more work is needed to confirm that some of these apparent differences are not due to surface features that are hidden in the Galinstan images.

The spray-containing region as a function of We can also be examined. At $\tau = 3$, bag breakup is relatively confined while sheet-thinning breakup shows a large spray width (Chou et al. 1997, Chou and Faeth 1998). Generally, the spray-containing region appears to be wider for Galinstan than water as

a function of τ. The same effect has been observed experimentally for conventional fluids with higher density ratios (Chou et al. 1997, Chou and Faeth 1998) undergoing various breakup regimes. Primary and secondary droplet motion drives the size of the spray-containing region. Thus, the underlying mechanisms controlling droplet motion differs from the column acceleration, requiring more detailed analysis illustrated later in Section 6.2.

4.2. Morphology Classification

A variety of experiments with water and Galinstan at different Weber numbers are classified in Fig. 5(a). In addition to experimental variability, inherent uncertainty exists in classifying breakup morphology from images, causing overlap where multiple morphologies can be observed. This is highlighted by the gray areas in Fig. 5. Overall, the breakup regimes match well for water and Galinstan, indicating that the Weber number can be used to classify Galinstan breakup morphology with cutoff points that match those of typical fluids with low Oh numbers. Interestingly, the transition Weber numbers of column breakup measured here are slightly lower than for spherical drop breakup, as summarized in Guildenbecher et al. (2009) and Kékesi et al. (2014). For the bag breakup regime, the critical transition Weber numbers We_{cr} are ∼5 to ∼6 for a column and ∼11 for a sphere. For the multi-mode regime the transition Weber numbers are ∼13 to ∼39 for a column and ∼18 to ∼35 for a sphere. However, in the sheet thinning regime, the transition weber numbers become more similar ($We \approx 82$ to 110 for a column, $We \approx 80$ for a sphere). This evidence suggests that column breakup behaviors may be different from canonical spherical drop breakup.

4.3. Characteristic Time Scales

Although the mechanisms driving sheet thinning and bag breakup are different, their initial deformation and breakup end times are relatively similar (Hsiang and Faeth 1992, Chou and Faeth 1998). The breakup initiation time τ_i is defined as the time when the column deforms away from a roughly oval cross section (Guildenbecher et al. 2009). This coincides with the column reaching a minimum width before expanding. The variation of τ_i as a function of We is plotted in Fig. 5(b) from the

Table 2: Bag Breakup Characteristic Times

Characteristic Time	Spherical Drops*	Water Column	Galinstan Column
Initial Deformation τ_i	∼2.0	2.7 ± 0.5	1.6 ± 0.4
Bag Growth $\Delta\tau_{bg}$	∼1.0	1.2 ± 0.7	0.8 ± 0.5
Breakup Initiation τ_d	∼3.2	3.9 ± 0.9	2.4 ± 0.7
Bag Breakup $\Delta\tau_{bb}$	∼1.0	0.9 ± 0.3	0.9 ± 0.1
Breakup End τ_e	∼5.0	7.2 ± 1.3	4.6 ± 1.4

*From Chou and Faeth (1998).

back-lit data. Some work in the literature suggests a decreasing breakup initiation time as the We increases (Pilch and Erdman 1987). By adding an extra offset constant, the form of the correlation is $\tau_i \approx C_{i1}(We - We_{cr})^{-1/4} + C_{i0}$. This functional form is fit to the data in Fig. 5(b). Although there is significant scatter, fitting produces $C_{i0} = 1.9$ and $C_{i1} = 1.1$ for water and $C_{i0} = 0.7$ and $C_{i1} = 0.9$ for Galinstan with a critical transition bag breakup Weber number of $We_{cr} \approx 5$. Alternatively, a simpler correlation (Hsiang and Faeth 1992) for the breakup initiation times of typical spherical fluid droplets indicate that $\tau_i \approx 1.6$ with no dependency on We. The average column breakup initiation times suggest that water breakup starts at $\tau_i = 2.4 \pm 0.6$ (mean and standard deviation) while Galinstan breakup starts at $\tau_i = 1.4 \pm 0.4$. The initiation times for Galinstan are again slightly earlier than for water.

Similarly, the observed breakup end times can also be compared with correlations from the literature with $\tau_e \approx 5$ (Hsiang and Faeth 1992). Here, the total breakup or end time occurs when fragmentation has stopped and all droplets are at their final size. For this expected breakup end time, the non-dimensional streamwise location at full breakup is quoted at $x_L/d_c \approx 40$ for the spherical drop core (Hsiang and Faeth 1993, Chou et al. 1997, Chou and Faeth 1998), where x_L is the upstream or left-most windward x-position of the core facing the flow. Simple linear curves were fit to the measured data, showing that $\tau_e = 0.021We + 7.00$ for water and $\tau_e = 0.036We + 4.97$ for Galinstan. Unlike existing correlations (Hsiang and Faeth 1992) that suggest a constant end breakup time for all Weber numbers of $\tau_e \approx 5.5$, both fluids here appear to have a weak upward trend for higher We.

The bag breakup regime has several other characteristic time scales that can also be compared for Galinstan and water as illustrated in Table 2, determined in a fashion similar to that in Chou and Faeth (1998). Here, the characteristic times are measured from a subset of the experiments in Fig. 5 that were classified under the bag breakup regime. For spherical drops, the breakup proceeds in multiple stages with initial deformation, bag growth, breakup initiation, bag breakup, and finally annular ring breakup (Chou and Faeth 1998). Experimentally, the characteristic time scales were found to be comparable for the two fluids, with slightly shorter and earlier breakup for Galinstan. Bag growth and bag breakup times, which are hypothesized to be driven by thin film breakup mechanisms (Chou and Faeth 1998), seem to match well for spherical and column geometries. However, the characteristic deformation, breakup initiation, and end times found for water column breakup occur slightly later than literature values for spherical drops.

4.4. Column versus Sphere Breakup

Based on current experimental results, column breakup appears to have a few features that make it unique when compared to more common spherical drop studies (Hsiang and Faeth 1992, Guildenbecher et al. 2017). Examples include differences in the transition regions for breakup morphology and

some characteristic breakup times. Igra and Takayama (2001) and Igra et al. (2002) explored column breakup and concluded that there are minimal differences between column and spherical drop breakup. However, the columns used in their work were low aspect ratio, where the length of the column was approximately the same size as the column diameter. In our current work, the liquid columns have a much larger length-to-diameter aspect ratio. We hypothesize that these geometric differences between our column aspect ratio and spherical drop aspect ratios from the literature will lead to differences in the transition Weber numbers, characteristic breakup times, and droplet size distributions.

First, the differences in transition Weber numbers noted in Section 4.2 can be explained by the geometric dependency of instabilities that drive breakup. For spherical drop breakup at low We (bag breakup regime) it is well established that the deformation is dominated by an instability in the cross-stream direction with wavelengths on the order of the droplet diameter (Theofanous et al. 2004). In the vertical cross-stream direction, a high aspect-ratio liquid column has different symmetry compared to a spherical drop. Therefore, one might expect this particular instability to show geometrical differences leading to earlier transition Weber numbers for columns. For example, a volume-weighted effective diameter can be calculated from the column diameter and the most unstable wavelength estimated by Rayleigh (1878) to produce $d_{eff} = 1.89 d_c$. If the bag breakup transition is $We \approx 11$ using d_{eff}, then the Weber number calculated using d_c for the same conditions would be $We \approx 5.8$. These results are similar to the transition Weber number differences seen for bag breakup of spherical versus column geometries.

On the other hand, at higher We (sheet thinning regime), the dominant instabilities of spherical drops tend to be in the stream-wise direction (Chou et al. 1997). In that direction, a sphere and column of the same diameter have the same surface curvature. Therefore, we hypothesize that high Weber numbers do not exhibit as many differences due to geometric effects.

High aspect ratio liquid columns contain a larger quantity of fluid than a spherical drop with the same characteristic diameter. A larger quantity of fluid allows for the formation of larger primary droplets, which can have larger characteristic diameters than the original column. These larger primary droplets may continue to breakup into secondary droplets via bag, multi-mode and sheet thinning mechanisms. This geometric effect will tend to extend the total breakup time beyond what is typically seen for spherical drops, as noted in Table 2 and Fig. 5(b). In addition, this effect will also make temporally separated breakup events (such as separate distinct times for bag and annular ring breakup for spherical drops as seen in Chou and Faeth 1998) appear more continuous and may obscure bimodal or tri-modal droplet size distributions typically seen for spherical drop bag breakup events (Guildenbecher et al. 2017).

5. Column Motion

Digital in-line holography is implemented to obtain more quantitative measurements of column motion and droplet sizes. Three different conditions were tested for each liquid at $We \approx 13$, 33 and 76 corresponding to the transition region from bag to multi-mode breakup, multi-mode breakup, and the transition region from multi-mode to sheet thinning breakup, respectively. The imposed gas velocities as a function of time are shown in Fig. 6(a). These velocities were measured in separate experiments inside an empty shock tube using pulse-burst particle image velocimetry in a manner similar to that described in Wagner et al. (2015). The free-stream plateau gas velocity, u_g, turbulence intensity, $u_T = \sqrt{\overline{u_g'^2}}/u_g$, initial column diameter, d_c, and gas densities after the shock, ρ_g, are listed in Table 3. The gas densities are estimated from experimentally measured pressure and flow conditions. Here, u_g' indicates the standard deviation of gas velocity. Column diameter deviations due to the capillary instability are captured by the d_c uncertainty values and are propagated into the estimated We.

Holography data was obtained at upstream $x_c \approx 0\ mm$, midstream $x_c \approx 25\ mm$ (centered at 25 mm for Galinstan, 22.2 mm for water), and downstream $x_c \approx 50\ mm$ locations with three experiments conducted at each position. The holography field-of-view is almost 8 mm wide for the 2× magnification and 3.4 mm wide for the 6× magnification. Since the column core generally contains the largest and slowest droplets that are most likely to break up at later non-dimensional times, the expected full breakup locations were predicted using the data in Fig. 5(b) and a column location model from Section 5.2. Based on this information, full breakup for $We \approx 13$ is predicted to occur before the 50 mm position while full breakup for the other two Weber numbers is predicted to occur after the 50 mm position. Therefore, a far-downstream location ($x_c \approx 98\ mm$) was tested for $We \approx 33$ and 76 to investigate the final drop size distributions after breakup is complete. After analysis, far-downstream Galinstan results appeared to be inconsistent due to mass loss as droplets hit the sides of the shock-tube. Thus, only far-downstream water results are included in this paper.

Table 3: Parameters for DIH experiments

Liquid	$u_g\ (m/s)$	u_T	$d_c\ (mm)$	$\rho_g\ (kg/m^3)$	We
Water	30 ± 2	0.8 %	0.94 ± 0.01	1.09	12.6 ± 1.9
Water	47 ± 2	0.8 %	0.94 ± 0.01	1.13	32.1 ± 3.1
Water	69 ± 2	0.8 %	0.94 ± 0.01	1.20	74.4 ± 5.0
Galinstan	80 ± 2	1.5 %	1.17 ± 0.18	1.22	12.7 ± 2.7
Galinstan	123 ± 2	1.5 %	1.17 ± 0.18	1.36	33.4 ± 6.5
Galinstan	177 ± 2	1.5 %	1.17 ± 0.18	1.56	79.5 ± 14.5

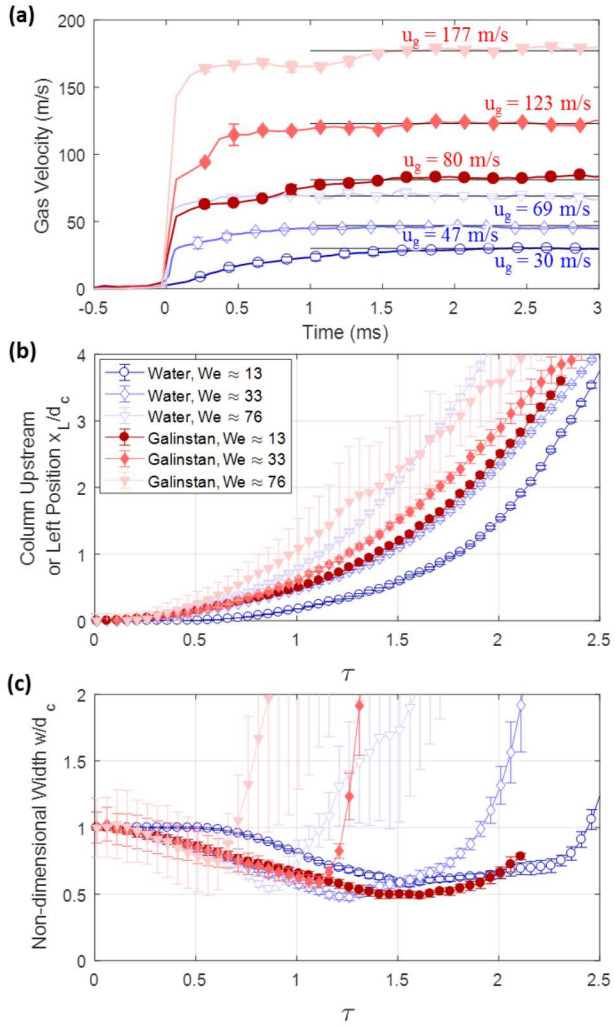

Figure 6: (a) Gas velocities following the shock arrival for the DIH test cases and the plateau gas velocities u_g are illustrated. Measurements were obtained using separate particle image velocimetry experiments in an empty shock tube. Error bars represent test-to-test standard deviation. (b) The non-dimensional upstream or left-most positions of the water and Galinstan columns are plotted as a function of non-dimensional time, indicating column acceleration. (c) The non-dimensional width of the columns are plotted as a function of non-dimensional time showing the initial compression of the column before breakup. Error bars in (b) and (c) indicate standard deviation along the column for a single test. (Figure available in color online)

5.1. Acceleration and Deformation

The DIH technique enables measurements of the evolution of the non-dimensional column upstream or left position x_L/d_c (Fig. 6(b)) and the non-dimensional width w/d_c (Fig. 6(c)) directly from high resolution column images (Fig. 7). Both Galinstan and water appear to have similar column acceleration as a function of non-dimensional time as indicated in Fig. 6(b). Note that the lowest We for water has a convective velocity that gradually rises over ∼0.5 ms, rather than nearly instantaneously with the shock boundary like the other conditions. This likely explains the lag seen in the acceleration of the column upstream or left position for the lowest water Weber number case since a constant convective

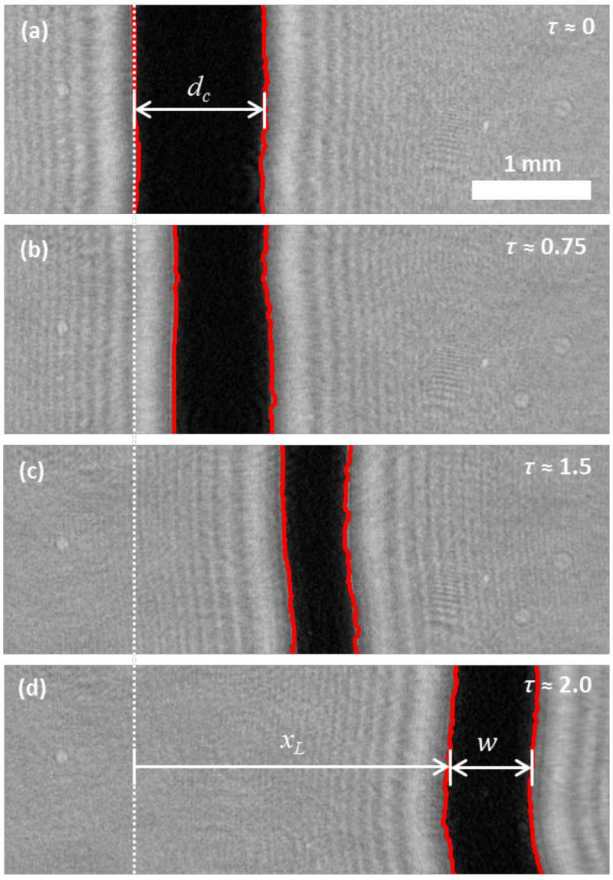

Figure 7: Initial column compression and acceleration during breakup is illustrated showing the column diameter, d_c, upstream or left position, x_L, and width, w, over time. This case shows Galinstan for $We \approx 13$ at (a) $\tau \approx 0$, (b) 0.75, (c) 1.5, (d) and 2.0, all numerically refocused to the center of the column.

velocity u_g is used to define τ.

With the exception of the lowest water Weber number case, all of the experiments show similar evolution in the non-dimensional widths up to $\tau = 0.5$. Some models assert that breakup initiation occurs when the column width approaches a particular minimum w/d_c ratio and expands (O'Rourke and Amsden 1987). Experimental investigations suggest that this breakup initiation time is a function of We (Pilch and Erdman 1987, Guildenbecher et al. 2009). Holography results in Fig. 6(c) indicate that the deformation appears to reach minimum ratios near w/$d_c = 0.5$ before expanding. Similar to Fig. 5(b), these results also suggest that breakup initiation time may decrease with increasing We for both fluids as predicted by Pilch and Erdman (1987), although this trend is more clearly visible in the DIH data than in the back-lit data. At higher Weber numbers, the minimum width of Galinstan appears slightly larger than for water, which may be due to sheet thinning occurring at the column edges before the column center is fully compressed. Overall, results show that Galinstan breaks up earlier than water by at least $\tau = 0.5$ for each Weber number condition.

5.2. Column Form Drag

Equation (2) provides a simplified representation of the column position as a function of time. A more detailed derivation which accounts for the changing drag force as the column velocity approaches the convective gas velocity can be achieved by using acceleration due to drag (Hsiang and Faeth 1993) and solving,

$$\frac{d\Delta u}{dt} = -\frac{1}{2} C_d \rho_g \Delta u^2 \frac{A}{M}, \tag{6}$$

where $\Delta u = u_g - u_{cx}$, u_{cx} is the column x-velocity, and $A/M = 4/(\pi \rho_l d_c)$. Following conventions in the literature, we assume that the column diameter, d_c, does not vary as a function of time to estimate bulk drag, $\overline{C_d}$. By integrating, using the initial condition $\Delta u = u_g$ at $t = 0$, and rearranging, the velocity of the column becomes,

$$\frac{u_{cx}}{u_g - u_{cx}} = \frac{2}{\pi} \overline{C_d} \tau \sqrt{\frac{1}{\rho^*}}. \tag{7}$$

The position of the column can be derived by solving $x_L = \int u_{cx} dt$ with initial condition $x = 0$ at $t = 0$ to give,

$$\frac{x_L}{d_c} = \frac{\pi \rho^*}{2\overline{C_d}} \left(\frac{2}{\pi} \overline{C_d} \sqrt{\frac{1}{\rho^*}} \tau - ln \left(\frac{2}{\pi} \overline{C_d} \sqrt{\frac{1}{\rho^*}} \tau + 1 \right) \right). \tag{8}$$

The functional form of this equation looks similar to the measured column positions for the higher We conditions in Fig. 6(b). For Galinstan, the best fit drag values are $\overline{C_d} \approx 2.1$, 2.4, 3.0 for at $We \approx 13$, 33, and 76, respectively, for early non-dimensional times. For water $\overline{C_d} \approx 1.9$, 2.2, 2.8 for $We \approx 13$, 33 and 76, respectively. Standard deviations of form drag curve fits for each test condition are approximately ± 0.3. From the data, the form drag appears to increase as the Weber number increases into the sheet thinning regime. This is most likely due to the assumption of a fixed diameter d_c over time when the true column cross section is actually deforming over time. As the Weber number increases, the deformation is more pronounced, which leads to higher $\overline{C_d}$. Observations in the literature have noted a correlation of $\overline{C_d} = 5$ for $We > 100$ in the sheet thinning regime (Hsiang and Faeth 1993), which extrapolates from our observations at lower We.

6. Droplet Characterization

Droplets are generated by primary breakup of the initial column and secondary breakup of larger primary droplets. Secondary breakup is a rate controlling process in dense sprays that drives droplet sizes and velocities (Chou et al. 1997). Characterization of droplet statistics via DIH is therefore essential to understanding the multiphase flow dynamics. The raw DIH images captured from the two different fields-of-view (FOV) are shown in Fig. 8(a) and (c). These images are first numerically refocused to maximize droplet edge sharpness, showing interesting non-spherical droplet shapes. These data are then used to calculate droplet diameter (by using the average projected area-equivalent diameter for each droplet across multiple frames) and velocity (via tracking across multiple frames), as

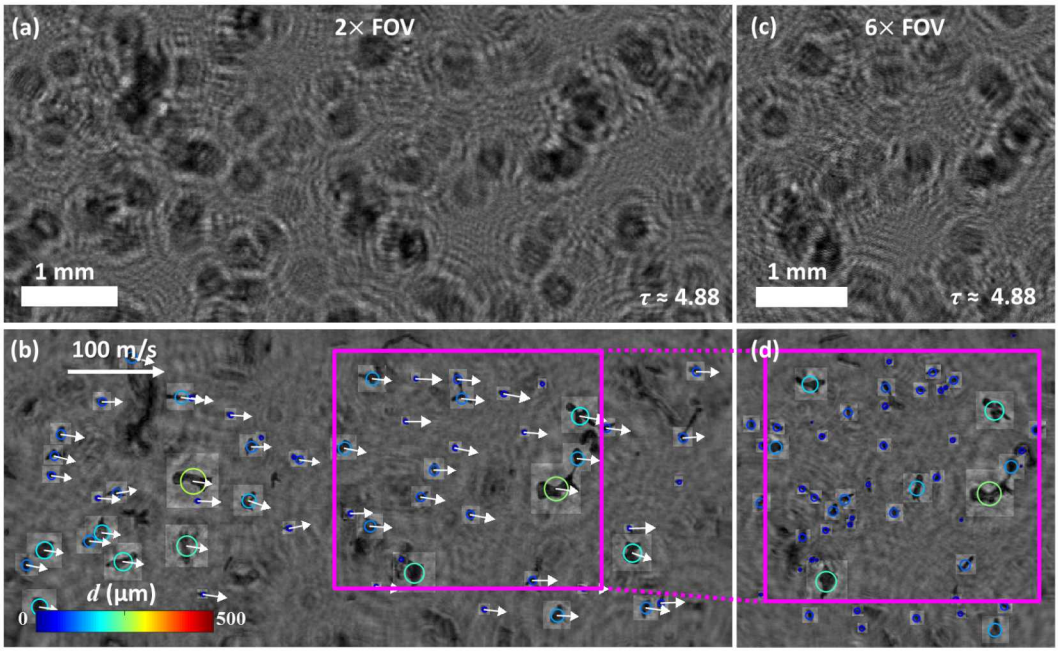

Figure 8: The raw and processed DIH images are shown for the two different camera views for Galinstan at $We \approx 13$ with a streamwise location of $x_c \approx 50\ mm$. (a) The raw 2× and (b) refocused ($z = 80\ mm$) magnification images are illustrated. The processed data includes images of each droplet refocused to its respective z-position (lighter boxes), estimates of droplet size, and video tracking estimates of droplet velocities. (c) The raw 6× and (d) refocused images for the same non-dimensional time are also shown. Magenta boxes signify matching areas between the two views. (Figure available in color online)

indicated in Fig. 8(b) and (d). Notice that the 6× FOV images are higher resolution and are therefore capable of identifying smaller droplets.

6.1. Three-dimensional Flow Profile

High speed digital in-line holography provides time-resolved measurements of droplet fields in three dimensions. Figure 9 shows examples of water and Galinstan at similar breakup stages (non-dimensional time shifted by $\tau \approx 0.5$) at a location of $x_c \approx 25\ mm$. A high-speed video summary of the DIH data for $We \approx 13$ at multiple streamwise locations for water and Galinstan is included with this paper in Video 2. In the earliest times, the initial bag breakup structures in water show small approximately spherical droplets, while string-like or web-like structures can be seen in the Galinstan breakup. In the intermediate time, larger and slower droplets begin to arrive. The smaller water droplets are more spherical while the larger water droplets are eccentric with rounded edges. On the other hand, all the Galinstan droplets appear to have sharp edges indicative of oxide film effects. Finally, at the latest times, the remainder of the intact column crosses the FOV.

In Fig. 9, the structures are examined in the x- and y-domains. In contrast to back-lit data where multiple perspective views are used to qualitatively estimate the z-direction profiles, DIH enables direct quantitative examination in the z-direction and Fig. 10 shows the corresponding x versus z plots. Here,

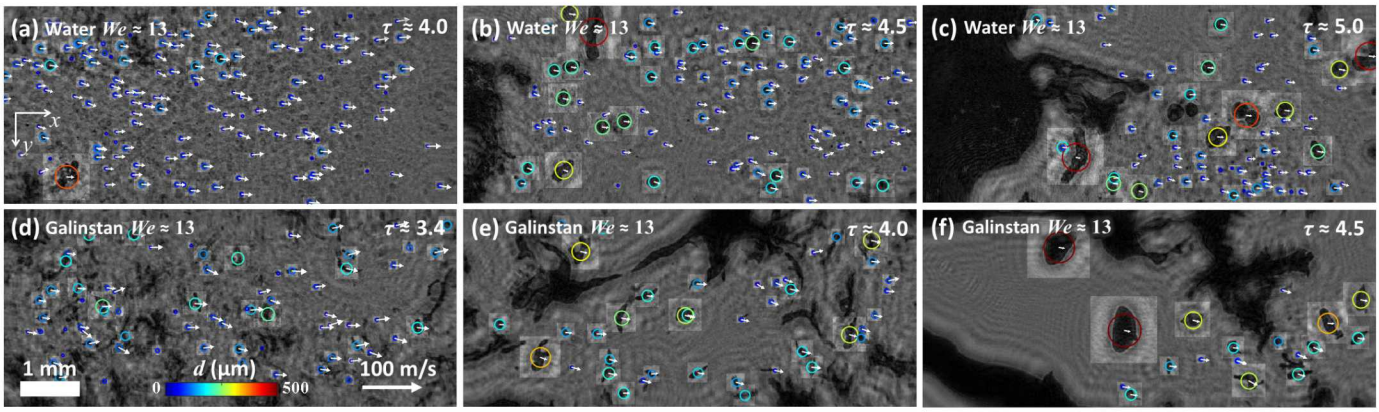

Figure 9: Comparison of refocused water (top row) and Galinstan (bottom row) holograms with droplet tracking at $We \approx 13$ at a streamwise location of $x_c \approx 25\ mm$. Galinstan breakup occurs $\tau \approx 0.5$ earlier than water, with droplet shapes that are more non-spherical. A high-speed video summary of the DIH data for $We \approx 13$ at multiple streamwise locations is included with this paper in Video 2. (Figure available in color online)

two sets of bag breakup structures are clearly visible for both liquids, showing evidence of multi-mode breakup behavior. Later in non-dimensional time, column breakup components are shown, with larger droplets (indicated in red) flanking the droplets in the center.

6.2. Size, Velocity and Time Scaling

Tracking individual droplets enables statistics to be collected on size and velocity, as shown in Fig. 11 for the three different Weber number cases. The gray dots in the first row show the typical variation of droplet sizes and velocities for a single case with water at $We \approx 13$ and $x_c \approx 50\ mm$. Only the average and standard error statistics are shown for the remaining cases. Initially, only the smallest and the fastest droplets are visible. As time progresses, larger and slower droplets appear. The first water droplets are tracked slightly later than Galinstan droplets by $\tau \approx 1.0$. The delay between the appearance of Galinstan and water droplets can be attributed to a combination of the earlier breakup of Galinstan, differences in convective velocity rise time to the plateau value, u_g, and the inability to track the smaller initial water droplets.

The cyan (dash-dot) and magenta (dashed) lines in Fig. 11 indicate the reflected shock arrival times for water and Galinstan respectively. For all of the experiments, the reflected shock arrives near the breakup end times τ_e (Fig. 5). Therefore, the reflected shock is not expected to heavily influence the droplet size distribution. However, it may have some effect on droplet velocities. Because removing data after the reflected shock would bias the size and size-velocity distributions, all of the data are included in the analysis and deviations are noted as they appear. The reflected shock has a minimal effect on particle velocities for $We \approx 13$ due to the lower convective velocities and weaker shocks. The reflected shock arrival does appear to have a slightly larger effect on the water data for $We \approx 33$ and $x_c \approx 98\ mm$. As illustrated later, velocity statistics for this dataset do deviate slightly from other

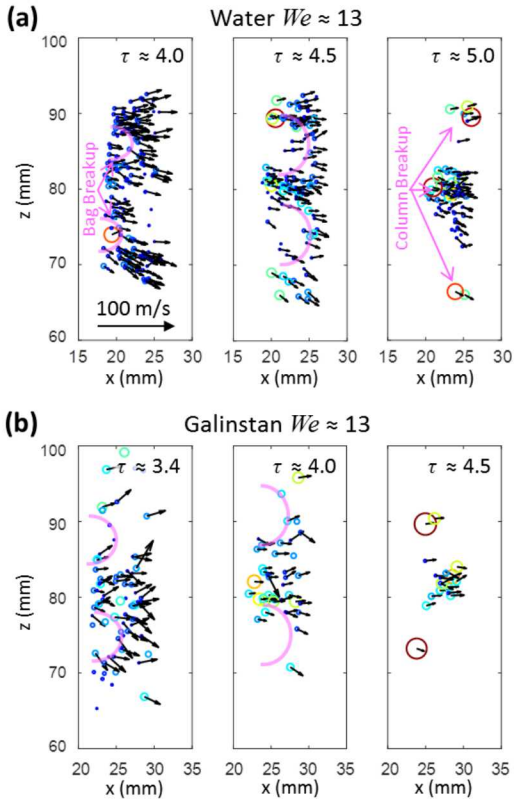

Figure 10: The z-depth dimension information shows breakup of a pair of multi-modal bags in both (a) water and (b) Galinstan at $We \approx 13$ with a streamwise location of $x_c \approx 25\ mm$. Magenta lines show the approximated locations of what appears to be fractured bag structures. Particle sizes are drawn 5× larger to improve visibility. (Figure available in color online)

experiments.

In terms of the non-dimensional velocity $u^* = u_x/u_g$, Galinstan droplets appear to be slower than water droplets at the same streamwise locations. Since the convective velocities u_g are higher for the Galinstan cases, it takes longer for droplets to match the gas velocities. Therefore, additional non-dimensionalization is needed to compare the droplet velocities of both fluids as seen from the fixed streamwise locations.

By comparing the left and right columns in Fig. 11, it is apparent that smaller initial droplets travel faster than larger drops at late times. This indicates a droplet size-velocity correlation. Some work in the literature shows no correlation between size and velocity (Chou et al. 1997). Other more recent work (Guildenbecher et al. 2017) shows weak size-velocity relationships similar to those observed in this paper. The droplet Reynolds numbers for these experiments range from 70 to over 15,000 depending on size and flow parameters. With a fixed flow velocity, smaller droplets experience a lower Reynolds number and therefore have higher drag forces approaching Stokes drag (Chou et al. 1997). These

droplets are therefore more likely to follow the local flow velocity. On the other hand, larger droplets have velocities equal that of the remaining column just prior to fragmentation.

The non-dimensional size-velocity correlations are shown in Fig. 12(a). Functional fits of the form $\hat{u}_x/u_g(d/d_c) = C_1 - C_2 e^{-C_3 d_c^2/d^2}$ from Chen and Guildenbecher (2017) and Powell et al. (2018) are fit to the water and Galinstan data. This functional form was derived from integrating the Stokes drag of a sphere assuming a constant gas velocity. Similar correlations for $\hat{u}_x(d)$ can also be used to correct for size-velocity biases in Section 6.3. For water, the constants after fitting $\hat{u}_x/u_g(d/d_c)$ were $C_1 = 0.55$,

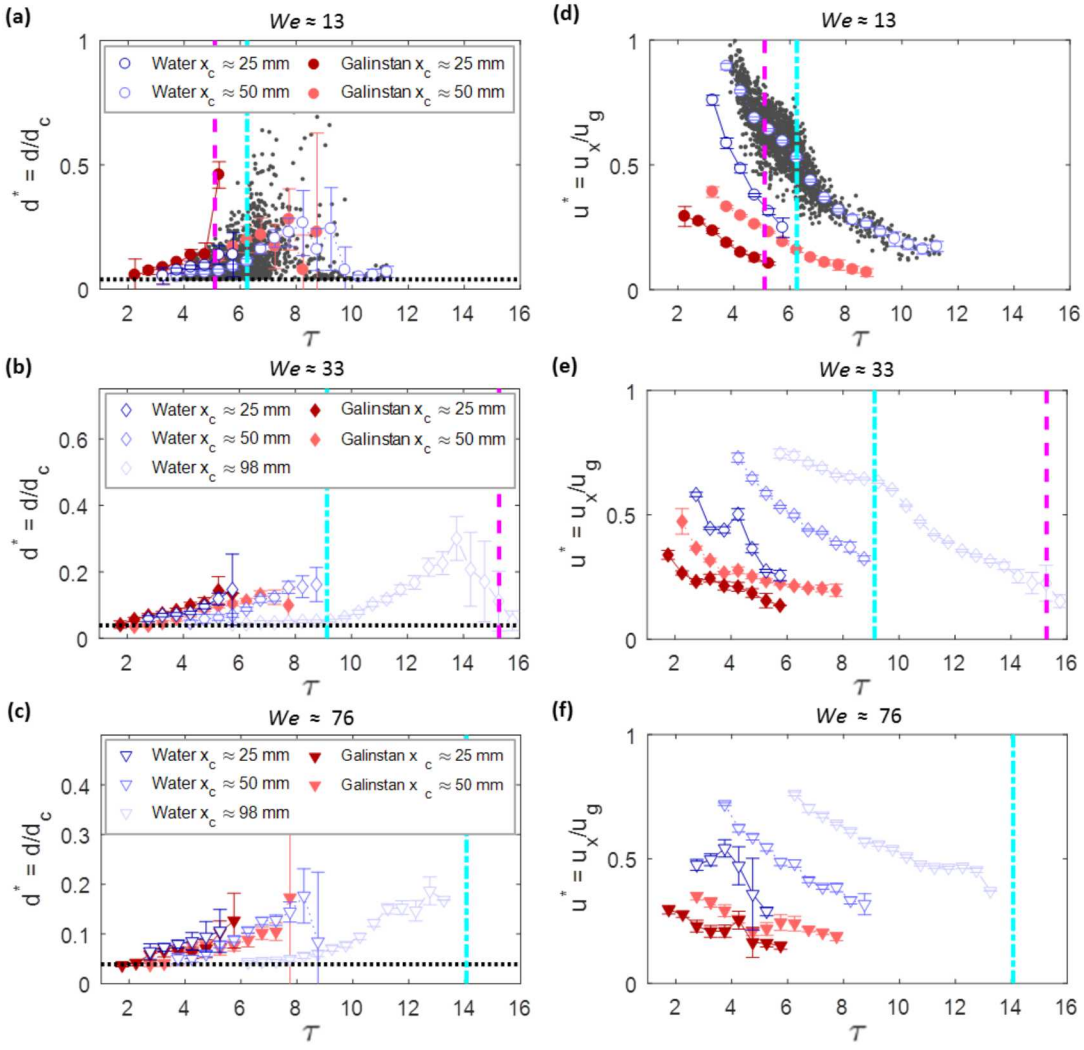

Figure 11: Droplet non-dimensional scaling for water and Galinstan is indicated for $We \approx 13$, 33, and 76 at multiple streamwise locations using the 2× magnification data. The non-dimensional diameter d^* is plotted as a function of the non-dimensional time τ in the first column as droplets pass by the camera FOV. The second column illustrates the non-dimensional velocity u^* as a function of non-dimensional time. Gray dots in the first row show the typical spread for droplet measurements from a single test case (water at $We \approx 13$ and $x_c \approx 50$ mm). Black dotted lines indicate the minimum measurable size (∼40 μm). The cyan (dash-dot) and magenta (dashed) lines indicate the reflected shock arrival for water and Galinstan, respectively. For water at $We \approx 33$ and 76, one additional far-downstream location is included. Error bars indicate the standard error of the mean for each time τ. (Figure available in color online)

$C_2 = 0.21$, and $C_3 = 0.011$. For Galinstan, the constants were $C_1 = 0.25$, $C_2 = 0.096$, and $C_3 = 0.015$. In this figure, two separate curves can be observed for the two fluids, with some variation as a function of streamwise location.

The theoretical behavior of droplets can be approximated and then derived in a manner similar to Eq.(7) with $A/M = 3/(2\rho_l d)$ for roughly spherical droplets. After substituting in τ and rearranging, this produces,

$$\frac{u_g - u_x}{u_x}\sqrt{\frac{1}{\rho^*}}\tau = \frac{4}{3C_{dd}}\frac{d}{d_c}, \tag{9}$$

which is similar to the solution derived by Hsiang and Faeth (1993), where u_x is the droplet x-velocity and C_{dd} is the form drag of a droplet. Figure 12(b) plots d/d_c against the left hand side of the equation and shows a reasonable collapse of the water and Galinstan data onto a single curve. This non-dimensionalization includes the effects of droplet size, droplet velocity, non-dimensional time, and the density ratio. As mentioned earlier, the case for water at $We \approx 33$ and $x_c \approx 98\ mm$ appears to be a slight outlier due to the reflected shock arrival time for this particular experiment.

A line can be drawn through the curve producing an estimate of the form $0.47d/d_c + 0.26$ on the right hand side of the equation. Hsiang and Faeth (Hsiang and Faeth 1993) note a similar effect, but instead of utilizing an offset, they use a power-law curve fit for the non-dimensional droplet diameter

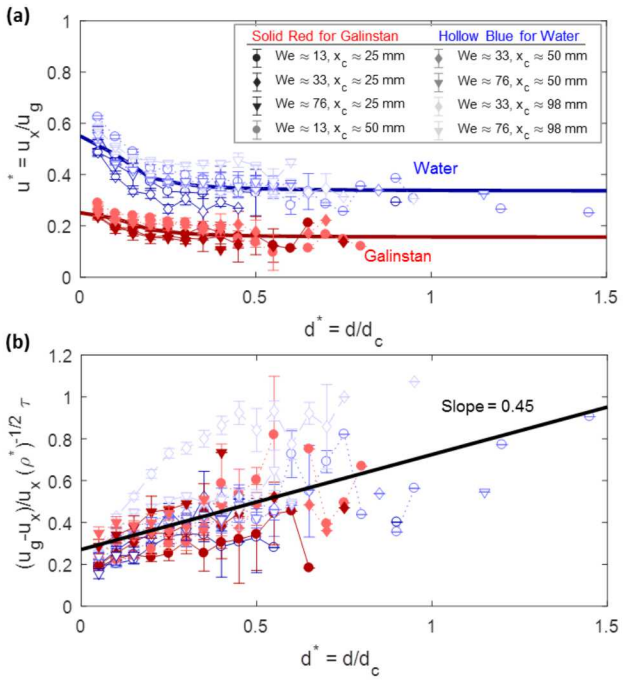

Figure 12: (a) The non-dimensional velocity u^* is compared with the non-dimensional diameter showing mostly the difference between the two fluids (water is shown in blue and Galinstan is shown in red). (b) Equation (9) can be plotted to non-dimensionalize the droplet diameter and velocity, successfully collapsing both fluids and multiple locations onto a single trend. Error bars indicate the standard error of the mean for each horizontal value. (Figure available in color online)

of the order $\sim(d/d_c)^{0.67}$. There are two potential sources of the offset. The first is an unknown initial droplet generation time and the second is an unknown initial droplet speed as it separates from the column. Experiments with a larger FOV capable of capturing the droplets throughout their evolution can provide more information for understanding droplet size-velocity scaling.

6.3. Droplet Size and Shape Distributions

Particle size distributions at varying streamwise locations can also be compared for the two fluids. Because the droplets are small and traveling at high velocities, trade-offs must be made in order to capture accurate droplet size distribution statistics with high dynamic range. Here, two fields-of-view are collected; one is temporally resolved (2× magnification, 100 kHz frame rate, minimum detectable droplet diameter $\sim$40 μm) with droplet tracking but low size dynamic range while the other is spatially resolved (6× magnification, 20 kHz frame rate, minimum detectable droplet diameter $\sim$12 μm) but has droplet displacements between frames that are too large for tracking.

Both magnifications contain some inherent bias. For the untracked, spatially resolved 6× magnification data, slower droplets will be over counted due to their longer residence time within the measurement volume. This type of bias can be corrected by multiplying the size distribution with the size-velocity correlations (Lefebvre 1989) similar to those found in Fig. 12(a). If the probability density (PD) of the spatially resolved data is $f_{6x}(d)$, and the size-velocity correlation is $\hat{u}_x(d)$, then the corrected PD from Chen and Guildenbecher (2017) is,

$$f^*_{6x}(d) = \frac{f_{6x}(d)\hat{u}_x(d)}{\sum f_{6x}(d)\hat{u}_x(d)}. \tag{10}$$

The temporally resolved 2× magnification data also contains biases due to its larger minimum detectable droplet size. If the measured temporally resolved PD is $f_{2x}(d)$, then the corrected temporally resolved 2× data (matching the corrected 6× data) is,

$$f^*_{2x}(d) = f_{2x}(d)\frac{\sum_{d=d_{2x,min}}^{d_{6x,max}} f^*_{6x}(d)}{\sum_{d=d_{2x,min}}^{d_{2x,max}} f_{2x}(d)}. \tag{11}$$

Since the size-velocity correlations are weak in these experiments, these corrections tend to be minor.

Figure 13 shows the corrected spatially resolved 6× high dynamic range droplet number and droplet volume probability distributions. Here, error bars for the number and volume distributions are calculated by assuming Poisson statistics for the probability of measuring droplets of a given size. Then the uncertainty of the size-velocity correlation is propagated through the number and volume probability density calculations. The number probability distributions show a weak bi-modal distribution with one peak at very small droplets and a second peak near 50 μm for all Weber number cases.

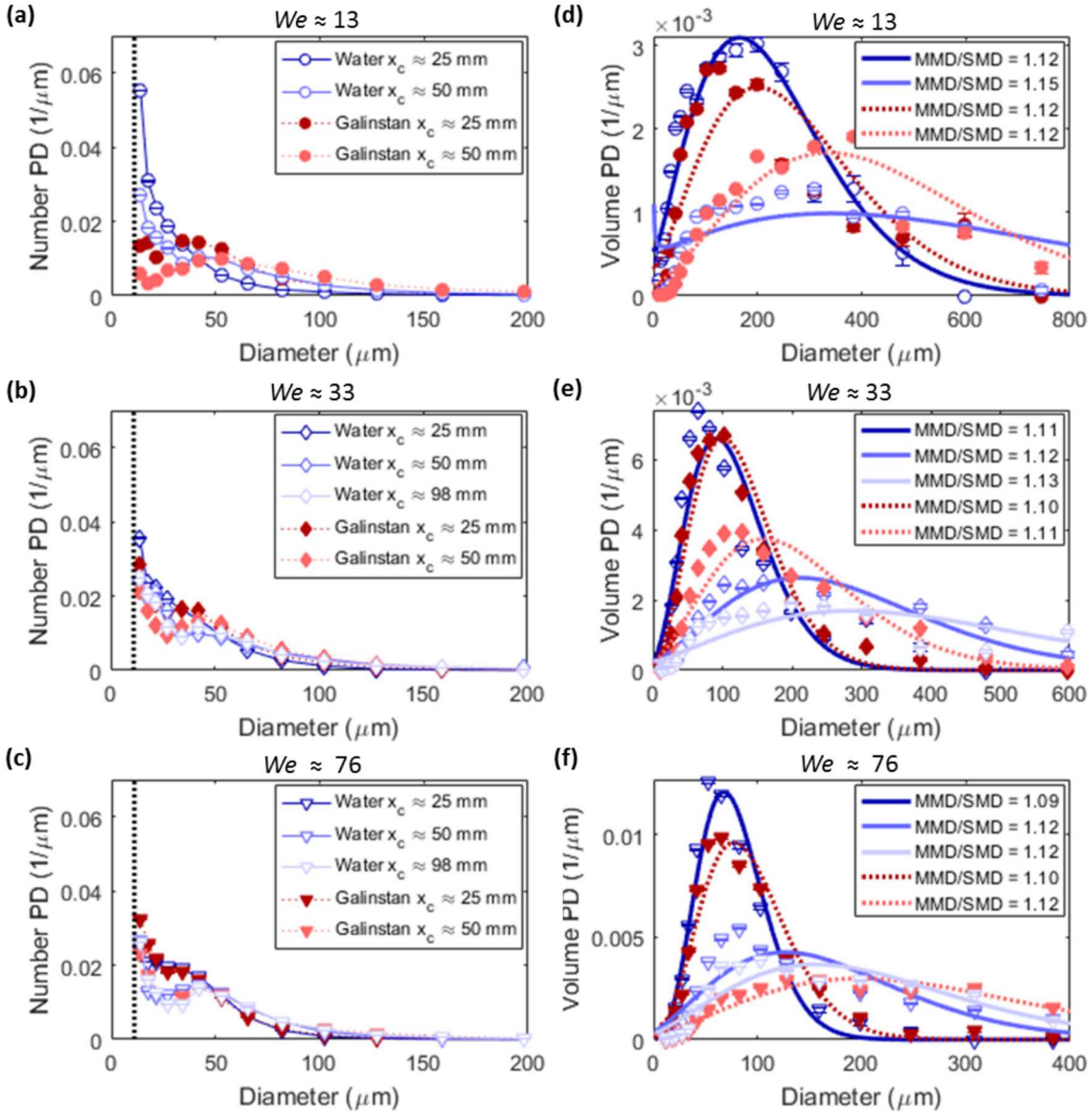

Figure 13: Corrected droplet number distribution (left column) and corrected volume distribution (right column) are indicated as a function of droplet diameter for the three different Weber number cases from the 6× magification data. The droplet volume distribution is fit with a Simmons root-normal distribution from Eq. (12), which can be described with a single MMD/SMD ratio. Standard error of the mean, which is small due to the large number of detected droplets, is plotted for each diameter interval. (Figure available in color online)

Volume PD results indicate that the detected average droplet volumes for both fluids increase as the Weber number decreases. Generally, the peak in the volume PD rises as the streamwise location increases up until the end of droplet breakup at the furthest streamwise locations. Existing literature suggests that the mean fragments sizes tend to increase with respect to non-dimensional time (Chou et al. 1997, Guildenbecher et al. 2017) and thus with streamwise location, which matches our current observations.

A Simmons root-normal distribution (Belz 1973, Simmons 1977) is often used to describe the volume PD in spray applications (Hsiang and Faeth 1992, Laney 2015). The root-normal distribution of the form,

$$f = \frac{C_f}{\sqrt{d/MMD}} exp\left(-\frac{1}{2S^2}(\sqrt{d/MMD}-1)^2\right) \tag{12}$$

is fit to the volume PD data in Fig. 13, showing a rough match to the overall shape. The root-normal distribution shape is characterized by a single non-dimensional number MMD/SMD, where the SMD and MMD are the bias-corrected Sauter mean diameter and mass mean diameter respectively, as defined in Section 6.5. This MMD/SMD ratio varies with standard deviation S in Eq.(12). Values were found to range from 1.04 to 1.5 in the literature (Hsiang and Faeth 1992, 1993, Chou and Faeth 1998).

For a fixed We, evidence suggests that the MMD/SMD is slightly smaller at earlier times and slightly larger for later times (Chou and Faeth 1998, Guildenbecher et al. 2017). The probability distribution fits in the right column of Fig. 13 show a slight increase in MMD/SMD at the further downstream locations. In addition, a decrease in MMD/SMD is also noted for higher Weber numbers, indicating slightly more uniform drop sizes. Chou and Faeth (1998) has noted that the root-normal distribution describes the sheet thinning regime better than the bag breakup regime, which can be bi-modal or tri-modal (Guildenbecher et al. 2017). However, in the current experiment with liquid columns, bi-modal and tri-modal behavior is not strongly visible. Overall, the probability distribution shapes and MMD/SMD ratios are similar for both fluids.

6.4. Mass Fraction Tracked as Droplets

Additional statistics characterizing the primary and secondary droplets are listed in Table 4. The number of droplets detected at the two different magnifications are shown; here $T_{2\times}$ indicates the number of trajectories tracked and $N_{6\times}$ indicates the number of droplets counted for each FOV. Each streamwise location and Weber number condition at the $N_{6\times}$ magnification contains more than 4000 droplet measurements, which are used for size distribution statistics.

The mass fractions tracked as droplets $M_{2\times}$ and $M_{6\times}$ are also listed with the standard deviation measured across multiple experiments. These values are calculated by comparing the volume of the tracked droplets with the original volume of the column within the FOV. The values are then corrected by accounting for the measured or predicted (via the size-velocity correlation) residence time of a droplet in the FOV as well as the probability of not counting a droplet at the edge of the FOV due to its size.

Since the 6× magnification has a higher dynamic range, does not reject droplets due to a lack of tracking matches, and is capable of capturing smaller droplets, it is believed to be a more accurate representation of the true mass fraction. As the column breaks up, more droplets will be generated

Table 4: Droplet count, tracked volume and corrected characteristic diameters (from 6× magnification data)

Liquid	We	midstream location $x_c \approx 25\ mm$								
		$T_{2\times}$	$N_{6\times}$	$M_{2\times}$ (%)	$M_{6\times}$ (%)	D_{10} (μm)	D_{30} (μm)	$D_{32}(SMD)$ (μm)	D_{43} (μm)	MMD (μm)
Water	∼13	1238	9953	10.9 ± 5.0	10.2 ± 1.8	35	71	146	269	210
Water	∼33	3314	12797	5.8 ± 0.4	7.5 ± 1.3	39	59	91	143	108
Water	∼76	1344	6529	0.9 ± 0.5	3.6 ± 1.2	39	51	67	86	75
Galinstan	∼13	2373	5244	13.0 ± 3.1	14.2 ± 9.8	58	102	187	394	251
Galinstan	∼33	5268	23134	6.0 ± 1.2	15.2 ± 1.3	47	68	100	171	117
Galinstan	∼76	2730	15006	1.4 ± 0.5	5.5 ± 0.8	40	55	75	103	87
Liquid	We	downstream location $x_c \approx 50\ mm$								
		$T_{2\times}$	$N_{6\times}$	$M_{2\times}$ (%)	$M_{6\times}$ (%)	D_{10} (μm)	D_{30} (μm)	$D_{32}(SMD)$ (μm)	D_{43} (μm)	MMD (μm)
Water	∼13	1845	13096	76.8 ± 35.0	64.5 ± 28.3	63	142	334	718	523
Water	∼33	2714	8709	38.5 ± 1.3	31.3 ± 20.9	60	110	195	297	258
Water	∼76	5523	10499	20.0 ± 2.2	21.7 ± 7.4	50	78	123	198	156
Galinstan	∼13	2016	4982	38.7 ± 4.7	48.8 ± 11.3	99	174	304	468	408
Galinstan	∼33	5725	23941	19.3 ± 3.3	37.9 ± 6.2	61	95	150	248	192
Galinstan	∼76	2599	15272	3.1 ± 1.7	43.5 ± 25.0	62	105	176	255	242
Liquid	We	far-downstream location $x_c \approx 98\ mm$								
		$T_{2\times}$	$N_{6\times}$	$M_{2\times}$ (%)	$M_{6\times}$ (%)	D_{10} (μm)	D_{30} (μm)	$D_{32}(SMD)$ (μm)	D_{43} (μm)	MMD (μm)
Water	∼33	2781	13959	59.4 ± 6.9	81.7 ± 25.8	58	119	253	530	361
Water	∼76	4159	12278	37.6 ± 5.0	42.5 ± 5.5	54	89	143	215	192

and a higher mass fraction will be tracked as droplets. This effect is evident in the back-lit data and in Table 4. In general, a larger mass fraction was tracked as droplets in the downstream $x_c \approx 50\ mm$ and far-downstream $x_c \approx 98\ mm$ locations than for the midstream location $x_c \approx 25\ mm$. Overall, the mass fractions are similar for water and Galinstan and generally more mass is tracked for the lowest Weber number condition.

6.5. Characteristic Mean Diameters

A variety of characteristic mean diameters with different weighting factors can be used to quantitatively describe polydisperse droplet distributions (Lefebvre 1989). Characteristic mean diameters are defined as,

$$D_{pq} = \left(\frac{\sum d^p}{\sum d^q} \right)^{\frac{1}{p-q}}, \tag{13}$$

and the size-velocity corrected 6× magnification values are,

$$D_{pq} = \left(\frac{\sum d^p \hat{u}_x(d)}{\sum d^q \hat{u}_x(d)} \right)^{\frac{1}{p-q}}. \tag{14}$$

The number population mean is D_{10}, the volume mean is D_{30}, the surface area weighted mean or Sauter mean is D_{32} (SMD), and the mean diameter over volume or DeBrouckere mean is D_{43}. The MMD is the diameter where half of the total measured mass is composed of drops of a larger diameter. The MMD can be directly corrected by weighting the mass of each droplet by its respective probability $\hat{u}_x(d)/\sum \hat{u}_x(d)$. The measured characteristic mean diameters for each DIH test case are compared in Table 4. Characteristic mean diameter uncertainty values can be derived following Lefebvre (1989) and are typically 0.5 to 2.8 μm in standard error (max 7.7 μm). One interesting point to note is that the MMD/SMD values obtained using this table are larger (on average ∼1.3) than for the fits found in right-hand column of Fig. 13. This indicates that there may be some small discrepancy from the root-normal distribution model.

At the ∼25 mm midstream location, Galinstan characteristic mean diameters are larger than water characteristic mean diameters. For multi-mode bag breakup at $We \approx 13$, Galinstan shows droplets that are significantly larger than water. Since the smallest droplets form first at this midstream location (and column breakup occurs further downstream), this result confirms the earlier hypothesis that Galinstan bags are thicker, thus producing initially larger droplets. The data for this streamwise location aligns with data from Fig. 9 that captures larger droplets for Galinstan.

At the ∼50 mm downstream location, the trends become more complex. Galinstan at $We \approx 13$ produces larger values for D_{10} and D_{30}, similar to the midstream condition, but smaller values for the remaining characteristic mean diameters. At this downstream location, column breakup has started to occur and the larger water droplets from column breakup can be measured for $We \approx 13$ and 33. However, the elastic surface oxides on Galinstan prevent oblong droplets from breaking up into separate droplets. This mechanism prevents the measurement of larger column breakup droplets in Galinstan for these two lower Weber number cases since accurate diameters and volumes cannot be obtained for large droplets that extend outside the FOV.

In the far-downstream location, the droplet sizes are larger than those in the downstream locations. Since full breakup has occurred at this location, the droplet size distributions should not change significantly further downstream unless droplets are lost via impact with the shock tube walls.

6.6. Drop Size Modeling

Droplet size models can be used to summarize multiple test conditions and compare the two fluids. Hsiang and Faeth (1992) derive a simplified shear breakup model for the droplet size distribution

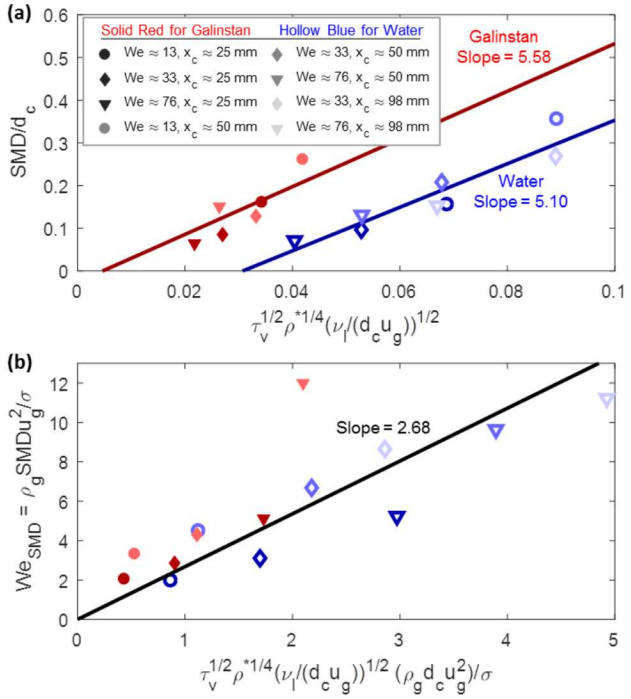

Figure 14: (a) The droplet size model SMD/d_c and (b) Weber number of the measured size distribution are plotted against the predictions by a shear breakup model. (Figure available in color online)

for high Weber numbers by assuming that the droplets scale with the size of the boundary layer thickness on the surface of the column. Although this model is derived specifically for high Weber number conditions, lower Weber number breakup regimes appear to coincidentally follow the same trends (Hsiang and Faeth 1992, Chou et al. 1997, Guildenbecher et al. 2009). Following conventions in the literature, this simple model is applied to provide predictions of the droplet size across multiple breakup regimes based on known properties, and is not used as an explanation for the underlying physics.

The model (Hsiang and Faeth 1992) is derived by assuming that the characteristic diameter scales with a boundary layer thickness at high We, giving $SMD/d_c = C_{st}(\nu_l t/d_c)^{1/2}$, where $\nu_l = \mu_l/\rho_l$ and C_{st} is an empirical scaling constant. After substituting for the non-dimensional time and rearranging, the droplet distribution becomes,

$$\frac{SMD}{d_c} = C_{st}\tau_v^{1/2}\rho^{*1/4}\left(\frac{\nu_l}{d_c u_g}\right)^{1/2}, \tag{15}$$

where τ_v is a volume weighted average for the droplet arrival time at each streamwise location. This equation can also be simplified to $SMD/d_c = C_{st}\tau_v^{1/2}\rho^{*1/4}Re_l^{-1/2}$. Figure 14(a) shows the results from both fluids at the three different conditions and several streamwise locations. From these trends, it is clear the Galinstan and water both collapse into their own separate curves. Galinstan appears to produce larger values of SMD/d_c for the same non-dimensional parameters $\tau_v^{1/2}\rho^{*1/4}Re_l^{-1/2}$. One

potential explanation is that Galinstan's slightly earlier breakup allows it to generate larger droplet distributions earlier in time, thus differentiating it from trends seen in typical fluids like water.

Both sides of Eq.(15) can then be multiplied by the Weber number in Eq.(1) to show the secondary atomization risk of the droplets (Hsiang and Faeth 1992),

$$\frac{\rho_g SMD u_g^2}{\sigma} = C_{st}\tau_v^{1/2}\rho^{*1/4}\left(\frac{\nu_l}{d_c u_g}\right)^{1/2}\frac{\rho_g d_c u_g^2}{\sigma}. \tag{16}$$

Note that this equation can be simplified to $We_{SMD} = C_{st}\tau_v^{1/2}\rho^{*1/4}Re_l^{-1/2}We$. Figure 14(b) shows the results for Galinstan and water indicating better overlap of the two fluids as inertial effects, via u_g^2, begin to dominate. A fit produced by (Hsiang and Faeth 1992) gives $C_{st}\tau_e^{1/2} = 6.2$ for $\tau_e = 5.5$. This further suggests that $C_{st} = 2.64$ for $We < 1000$ and $580 < \rho^* < 1000$. The fit in Fig. 14(b) for both fluids produces $C_{st} = 2.68$ for a higher density ratio range ($We < 76$ and $1000 < \rho^* < 5270$). The literature value and the value from these experiments are only off by 1.5%, showing a good match.

7. Conclusion

Liquid metal breakup processes occur commonly in manufacturing applications, metal combustion, and during explosive events. Galinstan enables the study of breakup at conditions that minimize the effect of temperature gradients, metal vapor pressure, and combustion effects. Liquids with atypical properties, such as non-Newtonian fluids, are often studied using the breakup framework of typical fluids like water (Mitkin and Theofanous 2017). By applying the same breakup framework to a liquid metal, we are able to investigate contributions of the high density ratio and elastic oxide layer formation. In particular, the fast oxide layer formation properties of Galinstan may provide some insights into breakup of other liquid metals like aluminum that have similar behaviors.

Fully decoupling the contributions of the density ratio and the elastic surface oxide presents significant difficulties. As both of these properties are fundamental to the liquid metals, it is more productive to think about the joint contributions of both properties. However, by investigating the column behaviors at early times before primary breakup occurs, it is possible to isolate some of the influence of the density ratio. At early times, the density ratio ρ^* affects the acceleration due to drag, deformation rates, and breakup morphology. Experimental results show that the breakup behaviors of the two fluids at different density ratios are very similar, with similar breakup transition Weber numbers, column acceleration rates, and initial non-dimensional widths (up to $\tau \approx 0.5$). At late times after breakup, we also show similar behavior in the size-velocity correlations of the two fluids after non-dimensionalization with ρ^*. Both fluids also appear to match root-normal volume probability distribution features. For these breakup properties, our results indicate a minimal effect caused exclusively by the density ratio. For other breakup properties, the influence of ρ^* is heavily coupled with the surface mechanics.

The effect of fast oxide formation on breakup properties is most visible in the breakup morphologies and droplet shapes. The amorphous oxide layer has a finite thickness on the order of 5 to 20 $\mathring{A}$ (Regan et al. 1997, Plech et al. 1998, Dickey 2014); this fundamentally limits the minimum size of the liquid droplets that can be formed and prevents bag deformation from achieving thin walls before breakup. During bag breakup, the oxide layer ruptures producing shapes more indicative of fracturing or yielding behavior than traditional surface tension-driven droplet beading behavior. A combination of the sustained velocity differentials from a higher ρ^* and elastic surface oxides drive column deformation and breakup to an earlier non-dimensional time. Galinstan appears to break up earlier (by $\tau \approx 0.5$ to 0.7) than water at the same Weber number, which in turn affects the size correlations, SMD/d_c.

Surface oxides also affect droplet shapes. At low Weber numbers, Galinstan droplet sizes are slightly larger and more non-spherical because surface oxide elasticity fights to retain existing shapes. Where water droplet shapes can become more spherical later in non-dimensional time and further downstream, the smallest Galinstan droplet shapes are unable to change shape once the oxide has formed. This is consistent with drop-impact results from the literature (Li et al. 2014), which suggest that the surface oxides help absorb energy and affect droplet shapes.

Interestingly, the choice of surface tension value does not heavily affect the differences noted between Galinstan and water related to earlier breakup or non-spherical droplet breakup morphologies. Surface tension also does not play a part in scaling laws related to droplet size, velocity, and probability distribution shape. Ultimately, using the effective surface tension values for Galinstan measured in the same oxygenated environment at similar timescales appears to be the most appropriate choice. Additional work in measuring Galinstan oxide-layer formation rates at short timescales would be valuable for understanding the underlying breakup mechanisms in more detail.

Liquid column breakup greatly simplified shock arrival timing and coordination with small camera fields-of-view. We hypothesize that the column breakup geometry is responsible for the observations of earlier transition Weber numbers, longer breakup times, more secondary breakup, and more mono-modal size distributions than for previous experiments with spherical liquid drops (Guildenbecher et al. 2017). However, by comparing matching conditions for liquid columns of both fluids, we were able to compare Galinstan and water effectively. Even though successful comparisons were made using traditional non-dimensional numbers such as We and τ, additional future work is needed to understand detailed breakup mechanisms and identify new scaling laws specifically for oxide-forming liquid metals.

Facility improvements to remove timing constraints, test time limitations, and non-ideal shock boundaries would provide additional capabilities for future experiments. Because the entire breakup event could not be captured by the small DIH field-of-view, it was appropriate to compare statistics as a function of streamwise location but more difficult to compare statistics as a function of time. Thus, future work may also focus on extending the current techniques to map time-dependent behaviors with

more streamwise locations.

This work is the first to explore the shock-induced breakup behavior of liquid metal Galinstan. Other than a single film-holography experimental data point with Mercury (Hsiang and Faeth 1992), shock-induced liquid metal breakup has not been investigated in the literature. Since mercury does not readily form surface oxides at room temperature (Li et al. 2014), its breakup behavior appears more similar to typical fluids like water (Hsiang and Faeth 1992) than other metals like aluminum that do form surface oxides. Here, high speed digital in-line holography videos and automated algorithms are used to obtain time-resolved droplet statistics. Results with an oxide-forming liquid metal elucidate behaviors that can be used to improve simulations of liquid metal breakup. Liquid metals have a variety of other interesting properties depending on their composition, and shock-induced breakup of these materials is a rich and under-explored research area. Additional studies that incorporate temperature, vapor pressure, and combustion effects would be important for understanding physics in explosives applications, metal combustion, and manufacturing processes.

Acknowledgment

The authors would like to thank M. Arienti for helpful discussions, K. P. Lynch his assistance with gas velocity measurements, and A. M. Turpin, S. W. Albert, and P. D. Sanderson for their assistance with experiments. The Sandia National Laboratories Scientific, Engineering and High Performance Computing group has kindly provided access to the ODIN MATLAB cluster. This work was supported by the Laboratory Directed Research and Development program at Sandia National Laboratories, which is a multimission laboratory managed and operated by National Technology and Engineering Solutions of Sandia, LLC., a wholly owned subsidiary of Honeywell International, Inc., for the U.S. Department of Energy's National Nuclear Security Administration under contract DE-NA0003525.

References

Aalburg, C., van Leer, B., Faeth, G. M., 2003. Deformation and drag properties of round drops subjected to shock-wave disturbances. AIAA J. 41 (12), 2371–2378.

Arienti, M., Chen, Y., Wagner, J. L., Guildenbecher, D. R., 2017. Aerodynamic breakup of liquid metal in a shock-induced crossflow. In: ILASS Americas 29th Annual Conference on Liquid Atomization and Spray Systems.

Arienti, M., Doisneau, F., Oefelein, J., 2016. Computation of the break-up of a molten metal drop under sudden acceleration. In: ILASS Americas 28th Annual Conference on Liquid Atomization and Spray Systems.

Belz, M. H., 1973. Statistical Methods in the Process Industries. Wiley, New York.

Chen, Y., DeMauro, E. P., Wagner, J. L., Arienti, M., Guildenbecher, D. R., Farias, P. A., Grasser, T. W., Sanderson, P. D., Albert, S. W., Turpin, A. M., Sealy, W., Ketchum, R. S., 2017a. Aerodynamic breakup and secondary drop formation for a liquid metal column in a shock-induced cross-flow. In: 55th AIAA Aerospace Sciences Meeting, AIAA SciTech. AIAA-2017-1892.

Chen, Y., Guildenbecher, D. R., 2017. Quantitative, bias-corrected measurements of droplet position, size and velocity with digital in-line holography. In: ILASS Americas 29th Annual Conference on Liquid Atomization and Spray Systems.

Chen, Y., Guildenbecher, D. R., Hoffmeister, K. N. G., Cooper, M. A., Stauffacher, H. L., Oliver, M. S., Washburn, E. B., 2017b. Study of aluminum particle combustion in solid propellant plumes using digital in-line holography and imaging pyrometry. Combust. Flame 182C, 225–237.

Chen, Y., Guildenbecher, D. R., Hoffmeister, K. N. G., Sojka, P. E., 2016. Digital imaging holography and pyrometry of aluminum drop combustion in solid propellant plumes. In: Proceedings of the Imaging and Applied Optics Conference: Laser Applications to Chemical, Security and Environmental Analysis. LT4F.2.

Chen, Y., Liang, X., Wei, S., Chen, X., Xu, B., 2012. Numerical simulation of the twin-wire arc spraying process: Modeling the high velocity gas flow field distribution and droplets transport. J. Therm. Spray Technol. 21 (2), 263–274.

Chou, W.-H., Faeth, G. M., 1998. Temporal properties of secondary drop breakup in the bag breakup regime. Int. J. Multiphase Flow 24, 889–912.

Chou, W.-H., Hsiang, L.-P., Faeth, G. M., 1997. Temporal properties of drop breakup in the shear breakup regime. Int. J. Multiphase Flow 23 (4), 651–669.

DeMauro, E. P., Wagner, J. L., Beresh, S. J., Farias, P. A., 2017. Unsteady drag following shock wave impingement on a dense particle curtain measured using pulse-burst PIV. Phys. Rev. Fluids 2, 064301.

Dickey, M. D., 2014. Emerging applications of liquid metals featuring surface oxides. ACS Appl. Mater. Interfaces 6 (21), 18369–18379.

Dickey, M. D., Chiechi, R. C., Larsen, R. J., Weiss, E. A., Weitz, D. A., Whitesides, G. M., 2008. Eutectic Gallium-Indium (EGaIn): A liquid metal alloy for the formation of stable structures in microchannels at room temperature. Adv. Funct. Mater. 18 (7), 1097–1104.

Dombrowski, N., Hooper, P. C., 1962. The effect of ambient density on drop formation in sprays. Chem. Eng. Sci. 17, 291–305.

Gao, J., Guildenbecher, D. R., Engvall, L., Reu, P. L., Chen, J., 2014. Refinement of particle detection by the hybrid method in digital in-line holography. Appl. Opt. 53 (27), G130–G138.

Gao, J., Guildenbecher, D. R., Reu, P. L., Chen, J., 2013. Uncertainty characterization of particle depth measurement using digital in-line holography and the hybrid method. Opt. Express 21 (22), 26432–26449.

Guildenbecher, D. R., Cooper, M. A., Gill, W., Stauffacher, H. L., Oliver, M. S., Grasser, T. W., 2014. Quantitative, three-dimensional imaging of aluminum drop combustion in solid propellant plumes via digital in-line holography. Opt. Lett. 39 (17), 5126–5129.

Guildenbecher, D. R., Cooper, M. A., Sojka, P. E., 2016a. High-speed (20 kHz) digital in-line holography for transient particle tracking and sizing in multiphase flows. Appl. Opt. 55 (11), 2892–2903.

Guildenbecher, D. R., Gao, J., Chen, J., Sojka, P. E., 2017. Characterization of drop aerodynamic fragmentation in the bag and sheet-thinning regimes by crossed-beam, two-view, digital in-line holography. Int. J. Multiphase Flow 94, 107–122.

Guildenbecher, D. R., Gao, J., Reu, P. L., Chen, J., 2013. Digital holography simulations and experiments to quantify the accuracy of 3D particle location and 2D sizing using a proposed hybrid method. Appl. Opt. 52 (16), 3790–3801.

Guildenbecher, D. R., López-Rivera, C., Sojka, P. E., 2009. Secondary atomization. Exp. Fluids 46 (3), 371–402.

Guildenbecher, D. R., Wagner, J. L., Olles, J. D., Chen, Y., DeMauro, E. P., Farias, P. A., Grasser, T. W., Sojka, P. E., 2016b. kHz rate digital in-line holography applied to quantify secondary droplets from the aerodynamic breakup of a liquid column in a shock-tube. In: 54th AIAA Aerospace Sciences Meeting, AIAA SciTech. AIAA-2016-1044.

Hsiang, L.-P., Faeth, G. M., 1992. Near-limit drop deformation and secondary breakup. Int. J. Multiphase Flow 18 (5), 635–652.

Hsiang, L.-P., Faeth, G. M., 1993. Drop properties after secondary breakup. Int. J. Multiphase Flow 19 (5), 721–735.

Hsiang, L.-P., Faeth, G. M., 1994. Drop deformation and breakup due to shock wave and steady disturbances. In: 32nd AIAA Aerospace Sciences Meeting, AIAA SciTech. AIAA-94-0560.

Hsiang, L.-P., Faeth, G. M., 1995. Drop deformation and breakup due to shock wave and steady disturbances. Int. J. Multiphase Flow 21 (4), 545–560.

Hussary, N. A., Heberlein, J. V. R., 2001. Atomization and particle-jet interactions in the wire-arc spraying process. J. Therm. Spray Technol. 10 (4), 604–610.

Igra, D., Ogawa, T., Takayama, K., 2002. A parametric study of water column deformation resulting from shock wave loading. Atomization Sprays 12, 577–591.

Igra, D., Takayama, A., 2001. Investigation of aerodynamic breakup of a cylindrical water droplet. Atomization Sprays 11, 167–185.

Joseph, D. D., Belanger, J., Beavers, G. S., 1999. Breakup of a liquid drop suddenly exposed to a high-speed airstream. Int. J. Multiphase Flow 25, 1263–1303.

Karcher, C., Kocourek, V., Schulze, D., 2003. Experimental investigations of electromagnetic instabilities of free surfaces in a liquid metal drop. In: International Scientific Colloquium: Modelling for Electromagnetic Processing. pp. 105–110.

Katz, J., Sheng, J., 2010. Applications of holography in fluid mechanics and particle dynamics. Annu. Rev. Fluid Mech. 42, 531–555.

Kékesi, T., Amberg, G., Prahl Wittberg, L., 2014. Drop deformation and breakup. Int. J. Multiphase Flow 66, 1–10.

Kim, D., Thissen, P., Viner, G., Lee, D.-W., Choi, W., Chabal, Y. J., Lee, J. B., 2013. Recovery of nonwetting characteristics by surface modification of gallium-based liquid metal droplets using hydrochloric acid vapor. Appl. Mater. Interfaces 5 (1), 179–185.

Kocourek, V., Karcher, C., Conrath, M., Schulze, D., 2006. Stability of liquid metal drops affected by a high-frequency magnetic field. Phys. Rev. E 74, 026303.

Kondo, S., Konishi, K., Isozaki, M., Imahori, S., Furutani, A., Brear, D. J., 1995. Experimental study on simulated molten jet-coolant interactions. Nucl. Eng. Des. 155 (1-2), 73–84.

Laney, C. B., 2015. Improved root normal size distributions for liquid atomization. Tech. Rep. DTRA-TR-16-3, Engility Corporation.

Lefebvre, A. H., 1989. Atomization and Sprays. Hemisphere Pub. Corp.

Li, H., Mei, S., Wang, L., Gao, Y., Liu, J., 2014. Splashing phenomena of room temperature liquid metal droplet striking on the pool of the same liquid under ambient air environment. Int. J. Heat Mass Transfer 47, 2–8.

Lin, M., Zhong, M., Li, Y., Yuan, M., Yang, Y., 2015. Numerical analysis on molten droplet hydrodynamic deformation and surface waves under high pressure pulse. Ann. Nucl. Energy 77, 133–141.

Ling, Y., Haselbacher, A., Balachandar, S., Najjar, F. M., Stewart, D. S., 2013. Shock interaction with a deformable particle: Direct numerical simulation and point-particle modeling. J. Appl. Phys. 113, 013504.

Liu, T., Sen, P., Kim, C.-J., 2010. Characterization of liquid-metal Galinstan® for droplet applications. In: IEEE 23rd International Conference on Micro Electro Mechanical Systems (MEMS). pp. 560–563.

Liu, T., Sen, P., Kim, C.-J., 2012. Characterization of nontoxic liquid-metal alloy Galinstan for applications in microdevices. J. Microelectromech. Syst. 21 (2), 443–450.

Luo, J., Qi, L.-H., Zhou, J.-M., Hou, X.-H., Li, H.-J., 2012. Modeling and characterization of metal droplets generation by using a pneumatic drop-on-demand generator. J. Mater. Processing Technol. 212 (3), 718–726.

Manickam, L., Bechta, S., Ma, W., 2017. On the fragmentation characteristics of melt jets quenched in water. Int. J. Multiphase Flow 91, 262–275.

Markus, S., Fritsching, U., Bauckhage, K., 2002. Jet break up of liquid metal in twin fluid atomisation. Mater. Sci. Eng. A326, 122–133.

Mates, S. P., Ridder, S. D., Biancaniello, F. S., Zahrah, T., 2012. Vacuum-assisted gas atomization of liquid metal. Atomization Sprays 22 (7), 581–601.

Mingjun, Z., Yuan, Z., Meng, L., Minghao, Y., Yanhua, Y., 2014. Numerical simulation of molten droplet deformation and disintegration under sudden accelerations. Ann. Nucl. Eng. 65, 199–206.

Mitkin, V. V., Theofanous, T. G., 2017. The physics of aerobreakup. I.V. strain-thickening liquids. Physics of Fluids 29, 122101.

Morley, N. B., Burris, J., Cadwallander, L. C., Nornberg, M. D., 2008. GaInSn usage in the research laboratory. Rev. Sci. Instrum. 79, 056107.

Newbery, A. P., Grant, P. S., 2013. Large arc voltage fluctuations and droplet formation in electric arc wire spraying. Powder Metall. 46 (3), 229–235.

O'Rourke, P. J., Amsden, A. A., 1987. The TAB method for numerical calculation of spray droplet breakup. In: Proc. International Fuels and Lubricants Meeting and Exposition. SAE Technical Paper, 872089.

Pilch, M., Erdman, C. A., 1987. Use of breakup time data and velocity history data to predict the maximum size of stable fragments for acceleration-induced breakup of a liquid drop. Int. J. Multiphase Flow 13 (6), 741–757.

Plech, A., Klemradt, U., Metzger, H., Peisl, J., 1998. In situ x-ray reflectivity study of the oxidation kinetics of liquid gallium and the liquid alloy $Ga_{0.93}Hg_{0.07}$. J. Phys.: Condens. Matter 10, 971–982.

Powell, M. S., Gunduz, I. W., Shang, W., Chen, J., Son, S. F., Chen, Y., Guildenbecher, D. R., 2018. Agglomerate sizing in aluminized propellants using digital inline holography and traditional diagnostics. J. Propul. Power [in press].

Rader, D. J., Benson, D. A., 1988. Aerosol production by high-velocity molten-metal droplets. Tech. Rep. SAND88-0678, Sandia National Laboratories.

Ranger, A. A., Nicholls, J. A., 1969. Aerodynamic shattering of liquid drops. AIAA J. 7 (2), 285–290.

Rayleigh, L., 1878. On the instability of jets. Proc. Lond. Math. Soc. 1 (1), 4–13.

Regan, M. J., Tostmann, H., Pershan, P. S., Magnussen, O. M., DiMasi, E., Ocko, B. M., Deutsch, M., 1997. X-ray study of the oxidation of liquid-gallium surfaces. Phys. Rev. B 55 (16), 10786–10790.

Simmons, H. C., 1977. The correlation of drop-size distributions in fuel nozzle sprays - Part I: The drop-size/volume-fraction distribution. J. Eng. Power 99 (3), 309–314.

Theofanous, T. G., Li, G. J., Dinh, T. N., 2004. Aerobreakup in rarefied supersonic gas flows. J. Fluid Eng. T. ASME 126, 516–527.

Wagner, J. L., Beresh, S. J., DeMauro, E. P., Casper, K. M., Guildenbecher, D. R., Pruett, B. O., Farias, P. A., 2016. Pulse-burst PIV measurements of transient phenomena in a shock tube. In: 54th AIAA Aerospace Sciences Meeting, AIAA SciTech. AIAA-2016-0791.

Wagner, J. L., Beresh, S. J., DeMauro, E. P., Casper, K. M., Pruett, B. O., Farias, P. A., 2015. Time-resolved PIV in a shock tube using a pulse-burst laser. In: 11th International Symposium on Particle Image Velocimetry.

Wagner, J. L., Beresh, S. J., Kearney, S. P., Trott, W. M., Castaneda, J. N., Pruett, B. O., Baer, M. R., 2012. A multiphase shock tube for shock wave interactions with dense particle fields. Exp. Fluids 52 (6), 1507–1517.

Yang, W., Jia, M., Sun, K., Wang, T., 2016. Influence of density ratio on the secondary atomization of liquid droplets under highly unstable conditions. Fuel 174, 25–35.

Yim, P., 1996. The role of surface oxidation in the break-up of laminar liquid metal jets. Ph.D. thesis, Massachusetts Institute of Technology.